University of Ioannina, Physics Department

Master Thesis

Onoufrios Sgouros

Transfer reactions for the system ^{20}Ne+^{28}Si at near barrier energies

Supervisor
Athena Pakou, Professor of Physics, University of Ioannina

Ioannina, May 2013

Review committee

Πανεπιστήμιο Ιωαννίνων, Τμήμα Φυσικής

Μεταπτυχιακή Διατριβή

Ονούφριος Σγούρος

Αντιδράσεις μεταφοράς για το σύστημα ^{20}Ne+^{28}Si σε ενέργειες κοντά στο φράγμα Coulomb

Επιβλέπουσα
Αθηνά Πάκου, Καθηγήτρια Φυσικής, Πανεπιστήμιο Ιωαννίνων

Ιωάννινα, Μάιος 2013

Τριμελής εξεταστική επιτροπή

Α. Πάκου, Καθηγήτρια Φυσικής, Πανεπιστήμιο Ιωαννίνων

Ε. Στυλιάρης, Αναπληρωτής Καθηγητής Φυσικής, Πανεπιστήμιο Αθηνών

Κ. Ιωαννίδης, Επίκουρος Καθηγητής Φυσικής, Πανεπιστήμιο Ιωαννίνων

Acknowledgements

I would like to thank all of those who have supported and assisted me during my graduate studies.

Professor of Nuclear Physics A. Pakou, my supervisor, for her guidance throughout my studies, for suggesting the subject, introducing me to the appropriate experimental and theoretical techniques and for supporting my efforts during my studies.

 The members of the Hellenic Institute of Nuclear Physics Professor A. Pakou, Associate Professor E. Stiliari, Lecturer N. Patroni, PhD candidate K. Zerva and my fellow worker Mr. V. Soukera for their generous assistance during the experiment.

I would like to express the deepest appreciation to the director of the Heavy Ion Laboratory of University of Warsaw (HIL), Professor K. Rusek, for making available the ICARE facility for the needs of our experiment and his generous hospitality in the dormitories of the laboratory during our stay in Warsaw.

I extend my sincere and warm thanks to: PhD candidate I. Strojek, Dr. A. Trzcinska and Dr. E. Piasecki for their support at the preparation and the performance of the experiment. I would also like to warmly thank the technical staff of HIL for providing good beams and for the support with electronics and the acquisition. Their help was more than useful.

I warmly thank Mr. Massimo Loriggiola from Laboratori Nazionali di Legnaro (LNL) for providing the silicon targets and Dr. M. Mazzocco from the University of Padova for his unreserved assistance during the preparation of the experiment.

Professor K. Rusek and Professor A. Pakou for introducing me in the *FRESCO* and *ECIS* calculations as well as Dr. N. Keeley for the theoretical support.

I would like to thank Associate Professor E. Stiliari and his students M. Mikeli, A. N. Rapsomaniki and M. Zioga for their help with the simulation code *GATE*.

Last but not least, I would like to thank my parents for supporting my efforts all these years and never stopped to have faith on me.

Ευχαριστίες

Θα ήθελα να ευχαριστήσω όλους όσους με στήριξαν και με βοήθησαν κατά τη διάρκεια των μεταπτυχιακών μου σπουδών.

Την Καθηγήτρια Πυρηνικής Φυσικής Α. Πάκου, για την καθοδήγηση κατά τη διάρκεια των σπουδών μου, για την πρόταση του θέματος της διατριβής, επειδή με εισήγαγε στις απαραίτητες πειραματικές και θεωρητικές μεθόδους και τέλος για την υποστήριξη των προσπαθειών μου καθ' όλη τη διάρκεια των σπουδών μου.

Τα μέλη του Ελληνικού Ινστιτούτου Πυρηνικής Φυσικής Καθηγήτρια Α. Πάκου, Αναπληρωτή Καθηγητή Ε. Στυλιάρη, Λέκτορα Ν. Πατρώνη, υποψήφια διδάκτορα Κ. Ζέρβα και τον συνεργάτη μου κ. Β. Σούκερα για την γενναιόδωρη βοήθεια τους κατά τη διάρκεια του πειράματος.

Θα ήθελα να εκφράσω την βαθύτατη εκτίμηση μου προς τον διευθυντή του Εργαστηρίου Βαρέων Ιόντων του Πανεπιστημίου της Βαρσοβίας (HIL), Καθηγητή Κ. Rusek, ο οποίος έθεσε στη διάθεση μας την γραμμή ICARE για τις ανάγκες του πειράματος, καθώς και για την γενναιόδωρη φιλοξενία του στους κοιτώνες του εργαστηρίου καθ' όλη τη διάρκεια παραμονής μας στη Βαρσοβία.

Εκτείνω τις θερμές ευχαριστίες μου στους: υποψήφια διδάκτορα Ι. Strojek, Δρ. Α. Trzcinska, και Δρ. Ε. Piasecki για την στήριξη τους κατά την προετοιμασία και την εκτέλεση του πειράματος. Θα ήθελα επίσης να ευχαριστήσω θερμά το τεχνικό προσωπικό του HIL που μας διασφάλισαν την βέλτιστη λειτουργία του επιταχυντή και για την βοήθεια τους στα οποιαδήποτε ζητήματα ανέκυψαν με τις ηλεκτρονικές μονάδες. Η βοήθεια τους ήταν κάτι παραπάνω από χρήσιμη.

Ευχαριστώ θερμά τον κ. Massimo Loriggiola από το Εθνικό Εργαστήριο του Legnaro (LNL) ο οποίος κατασκεύασε του στόχους πυριτίου και τον Δρ. Μ. Mazzocco από το Πανεπιστήμιο της Πάβδας για την αμέριστη βοήθεια που μας παρείχε κατά την προετοιμασία του πειράματος.

Τον Καθηγητή Κ. Rusek και την Καθηγήτρια Α. Πάκου οι οποίοι με βοήθησαν να εξοικειωθώ με τους υπολογιστικούς κώδικες *FRESCO* και *ECIS,* καθώς και τον Δρ. Ν. Keeley για την θεωρητική υποστήριξη που μας παρείχε.

Θα ήθελα να ευχαριστήσω τον Αναπληρωτή Καθηγητή Ε. Στυλιάρη και τους φοιτητές του Μ. Μικέλη, Α. Ν. Ραψωμανίκη και Μ. Ζιώγα για την βοήθεια τους σχετικά με τον κώδικα προσομοίωσης *GATE.*

Τέλος, θα ήθελα να ευχαριστήσω τους γονείς μου που στηρίζουν τις προσπάθειες μου όλα αυτά τα χρόνια και που ποτέ δεν σταμάτησαν να έχουν πίστη σε εμένα.

Contents

Abstract

The present work refers to the study of transfer reactions for the system ^{20}Ne+^{28}Si at near barrier energies, namely at 52.3 and 70 MeV. The experiment was visualized at ICARE target facility of the Heavy Ion Laboratory of the University of Warsaw. ICARE chamber hosts two independent rotating platforms and several rings, for setting up numerous detectors. A ^{20}Ne beam, delivered from the U-200P Cyclotron, bombarded a 200μg/cm^2 silicon target, placed perpendicular to the beam direction, and the various ejectiles were collected in an angular distribution measurement by three gas telescopes, able to discriminate the reaction products from the elastic ones by the conventional ΔE-E technique. The two stage telescopes were consisting of a gas detector filled with isobutane at a pressure of 15 mb, followed by a 500 μm silicon detector. Also, single silicon detectors were used at the more backward angles where both elastic and transfer channel cross sections are expected to be low. Two single detectors, served as monitors, were set at ±20° for normalization purposes.

The spectra analysis was performed with the code *PAW*. Based on the energy calibration of the detectors, the kinematics and the energy loss of the colliding ions, one alpha striping and pick up reaction products as well as a whole ^{8}Be transfer from the projectile to the target were identified in a ΔE-E process and differential cross sections were formed. The analysis of the experimental data was performed in the *DWBA* framework using the code *FRESCO* for calculating transfer reaction transition amplitudes. The basic ingredients required to calculate the transfer amplitude in the *DWBA* approximation is the interacting potentials and the wave functions for the initial and final states. As the effective potential, responsible for the transfer process, acts only on the transferred particle wave function, a cluster model was adopted in both entrance and exit channel where, the projectile is assumed to be a valence particle bound to a core nucleus. Into this context, the appropriate binding potentials were taken from the literature. As for the entrance potential, where the transfer calculations proved to be strongly dependent, three potentials were considered, deduced from a parallel analysis performed in this laboratory in reference with elastic scattering angular distribution data. Two described by a *Woods-Saxon* form factor for the real part,-one with a deep and one with a shallow depth- and a microscopic one adopting the *BDM3Y1* interaction. *Woods-Saxon* form factors were also adopted for the imaginary part of all three optical potentials.

These potentials were fed as entrance potentials to the transfer channel calculations, to verify their validity. At the energy of 52.3 MeV, in general, the agreement with the data was satisfactory with best agreement obtained with the microscopic potential. At the energy of 70 MeV, some inconsistencies between the experimental and the predicted transfer cross sections were clear, but without strongly affecting the validity of the proposed potential.

Finally, more elaborated calculations were performed in the *Coupled Reaction Channels* framework by Dr. Nick Keeley and were adopted in this work, providing a better description of the transfer angular distributions than the simple *DWBA* calculations.

Περίληψη

Η παρούσα μεταπτυχιακή εργασία αφορά την μελέτη των αντιδράσεων μεταφοράς για το σύστημα ^{20}Ne+^{28}Si με μετρήσεις και υπολογισμούς γωνιακών κατανομών σε ενέργειες κοντά στο φράγμα Coulomb και συγκεκριμένα στα 52.3 και στα 70 MeV. Το πειραματικό μέρος της μελέτης πραγματοποιήθηκε στην γραμμή ICARE του Εργαστηρίου Βαρέων Ιόντων του Πανεπιστημίου της Βαρσοβίας (HIL). Στη γραμμή αυτή ο θάλαμος ICARE, διαθέτει δυο ανεξάρτητα περιστρεφόμενες πλατφόρμες καθώς και αρκετές βάσεις σε σχήμα δακτυλίου, περιβάλλουσες τις πλατφόρμες, επιτρέποντας την τοποθέτηση πολλών ανιχνευτών.

Στο παρών πείραμα στόχοι ^{28}Si, πάχους 200 μικρογραμμαρίων ανά τετραγωνικό εκατοστό, βομβαρδίστηκαν με δέσμη ιόντων ^{20}Ne, παραγόμενη από το κυκλοτρόνιο U-200P του Εργαστηρίου HIL- Βαρσοβίας. Τα διάφορα προϊόντα αντιδράσεων ανιχνεύτηκαν κυρίως από τρία τηλεσκόπια με βάση την γνωστή τεχνική ΔΕ-Ε. Τα τηλεσκόπια αποτελούνται από 2 μέρη. Το πρώτο είναι ένας ανιχνευτής αερίου, περιέχων ισοβουτάνιο σε πίεση 15mb, ενώ το δεύτερο είναι ένας ανιχνευτής πυριτίου πάχους 500 μικρομέτρων. Επίσης, απλοί ανιχνευτές πυριτίου χρησιμοποιήθηκαν στις πιο πίσω γωνίες όπου η ενεργός διατομή του ελαστικού καναλιού αλλά και των καναλιών αντιδράσεων μεταφοράς αναμένεται μικρή, ενώ δυο από αυτούς τοποθετήθηκαν μπροστά, στις $\pm20^{o}$ για τον υπολογισμό της ροής της δέσμης.

Η ανάλυση των φασμάτων πραγματοποιήθηκε με τη χρήση του κώδικα *PAW*. Με βάση τα αποτελέσματα της ενεργειακής βαθμονόμησης των ανιχνευτών, τις κινηματικές των αντιδράσεων και την απώλεια ενέργειας των ιόντων μέσα στους ανιχνευτές, ταυτοποιήθηκαν προϊόντα που προέκυψαν από την μεταφορά ενός σωματίου άλφα από και προς το βλήμα, καθώς και από τη μεταφορά ενός ολόκληρου πυρήνα ^{8}Be από το βλήμα στο στόχο με την τεχνική ΔΕ-Ε και προσδιορίστηκαν οι αντίστοιχες διαφορικές ενεργές διατομές. Η ανάλυση των πειραματικών δεδομένων έγινε υιοθετώντας την *Προσέγγιση Born Παραμορφωμένου Κύματος* με τη βοήθεια του υπολογιστικού κώδικα *FRESCO*. Τα απαραίτητα στοιχεία που απαιτούνται για να υπολογιστεί το πλάτος πιθανότητας των αντιδράσεων μεταφοράς στην προσέγγιση αυτή είναι τα δυναμικά αλληλεπίδρασης καθώς και οι κυματοσυναρτήσεις των αρχικών και τελικών καταστάσεων. Επειδή το δυναμικό που ευθύνεται για την αντίδραση μεταφοράς δρα μόνο πάνω στην κυματοσυνάρτηση του μεταφερόμενου σωματιδίου, υιοθετήθηκε ένα μοντέλο *συσσωματώματος* και για το κανάλι εισόδου και για το κανάλι εξόδου, όπου το βλήμα λαμβάνεται ως ένας κεντρικός πυρήνας δέσμιος με ένα σωμάτιο σθένους. Στο πλαίσιο αυτό τα απαραίτητα δυναμικά συνοχής (binding potentials) ελήφθησαν από την βιβλιογραφία. Όσον αφορά το δυναμικό εισόδου, στο οποίο ο υπολογισμός φάνηκε να έχει ισχυρή εξάρτηση, χρησιμοποιήθηκαν τρία δυναμικά ως αποτέλεσμα μιας παράλληλης ανάλυσης στο εργαστήριο μας, των αντίστοιχων δεδομένων γωνιακής κατανομής ελαστικής σκέδασης. Στα δυο πρώτα δυναμικά, το πραγματικό μέρος του οπτικού δυναμικού περιγράφεται από ένα δυναμικό τύπου *Woods-Saxon*, ένα με βαθύ και ένα με ρηχό

βάθος πηγαδιού, ενώ για το τρίτο υιοθετήθηκε η αλληλεπίδραση *BDM3Y1*. Σε όλες τις περιπτώσεις, το φανταστικό μέρος του οπτικού δυναμικού περιγράφηκε με ένα δυναμικό τύπου *Woods-Saxon*.

Εν συνεχεία, τα αποτελέσματα αυτά χρησιμοποιήθηκαν σαν δυναμικά εισόδου στους υπολογισμούς των ενεργών διατομών των αντιδράσεων μεταφοράς προκειμένου να επαληθευτεί η εγκυρότητά τους. Για την ενέργεια των 52.3 MeV, η συμφωνία των υπολογισμών με τα δεδομένα είναι εν γένει ικανοποιητική. Η καλύτερη περιγραφή όμως επετεύχθη με χρήση μικροσκοπικού δυναμικού στο κανάλι εισόδου. Στην περίπτωση των 70MeV, υπάρχουν κάποιες αποκλίσεις μεταξύ των πειραματικών και των προβλεπόμενων ενεργών διατομών, χωρίς όμως να αμφισβητείται η εγκυρότητα των δυναμικών που περιγράφουν την ελαστική σκέδαση στο κανάλι εισόδου.

Τέλος, στην παρούσα εργασία συμπεριλαμβάνονται και κάποιοι πιο ακριβείς υπολογισμοί που πραγματοποιήθηκαν στο πλαίσιο της τεχνικής των *Συζευγμένων Καναλιών Αντιδράσεων* από τον Δρ. Nick Keeley. Οι υπολογισμοί αυτοί παρέχουν εν γένει καλύτερη περιγραφή των ενεργών διατομών σε σύγκριση με τους απλούς υπολογισμούς της *Προσέγγισης Born Παραμορφωμένου Κύματος*.

Introduction

This work is part of the curriculum of the Postgraduate Program of the Department of Physics, University of Ioannina. The research area belongs to the basic direction of Nuclear Physics and in particular in the area of Nuclear Reactions.

Transfer reactions traditionally are used as the main tool to probe nuclear structure. In this respect, the results obtained from the study of the (d, p) stripping reactions, involving single-neutron transfer, helped to validate the nuclear shell model [1]. Furthermore, transfer reactions have been of critical importance for the study of the α-clustering in nuclei. The (^{6}Li,d) reactions are excellent candidates for this purpose, as they take place mainly on the nuclear surface. The α-cluster states in ^{44}Ti [2] or ^{40}Ca [2] have been studied via ^{6}Li induced reactions where, the cross sections analysis yielded information about the α-cluster states of the specific nuclei. From the astrophysical point of view, transfer reactions like the ^{12}C (^{7}Li, t) ^{16}O [3] provide α particle widths, a fundamental information to calculate the ^{12}C (α, γ) ^{16}O [4] capture rate and thus, the mass fraction of ^{12}C and ^{16}O in the stellar evolution. Finally, cluster spectroscopic factors may be evaluated through transfer reactions, by comparing the calculated differential cross sections with the experimental data.

A general characteristic of all transfer processes is that the transfer probability is strongly dependent from the entrance potential. This was the basic motive for the present work here where, transfer reaction studies have been adopted as the tool for validating optical potentials deduced in a parallel analysis of the elastic scattering data.

From systematic studies on heavy ions collisions [5-11], it is known that the elastic scattering angular distribution presents a diffraction structure with increasing angle. This phenomenon is significant only in systems where both projectile and target present cluster structure. Several explanations have been introduced to explain this behavior, from surface transparent optical potentials [12] and couplings to peripheral reactions to the interference between near side and far side waves [13]. At near barrier energies, considering the cluster structure of the involved nuclei, mechanisms based on nucleus transfer or elastic transfer [14-16] may be the most prominent tool in order to explain the back angle "anomaly" of the elastic scattering cross section.

In the most reaction models, transfer reaction amplitudes are depended both on the entrance and exit potential. For example, in the distorted wave model where the relative motion between the nuclei at the entrance and the exit channel is described by distorted waves, it is critical to know the potential which describes the nucleus-nucleus interaction in order to evaluate the distorted wave functions. The dependence of the transfer cross section from the choice of the elastic scattering potential was tested by R. Bock and H. Yoshida [17]. They performed some trial calculations where, instead for the entrance channel potential, they adopted the exit channel one and vice versa. It was found that both the shape of the transfer angular distribution and the

cross sections magnitudes were changed. So, the choice of the appropriate optical potential may affect the transfer channel calculations.

The analysis of transfer nuclear reactions has been long described by procedures such as the *Distorted Wave Born Approximation* (*DWBA*) or the *Coupled Reaction Channel* (*CRC*) [18]. For the *DWBA* calculation coupling is ignored while, the (uncoupled) elastic distorted wave functions are used to determine the transfer amplitude. Although the *DWBA* approximation can be regarded as the weak coupling limit of the *CRC* one, its applicability has been tested in various transfer reaction, involving light nuclei like ^{12}C (^{6}Li, d) ^{16}O [19] or heavier ones such as ^{24}Mg (^{16}O,^{12}C) ^{28}Si [20], with satisfactory results. Also, the study of transfer reaction between heavy ions e.g ^{11}B (^{16}O, ^{15}N) ^{12}C [21] or ^{16}O(t, p)^{18}O and ^{12}C (t, p) ^{14}C [22], confirmed that the *DWBA* calculation is sensitive to the choice of the optical potential providing a reasonable test for its validity.

The team of Nuclear Physics Laboratory at the Physics Department of the University of Ioannina in recent years is dealing with the study of elastic scattering and nuclear reactions at near barrier energies in interplay between them, for obtaining the optical potential [23-37]. This research is systematic and devoted so far, to studies with weakly bound light projectiles on the same target ^{28}Si. Extending these studies to heavier projectiles presenting a cluster structure, it was proposed the study of the transfer channels in ^{20}Ne+^{28}Si at near barrier energies, as a complementary tool to the elastic scattering for probing the optical potential. The relevant experiment was performed in the Heavy Ion Laboratory of University of Warsaw at the beam energies of 52.3 and 70MeV. The analysis of the data was completed at the NPL − Ioannina and the results are discussed in the present work, which includes the following chapters:

- Chapter 1: Includes the theoretical background that is a brief description of the direct nuclear reaction mechanisms as well as extensive report of the *DWBA* procedure.

- Chapter 2: Includes details of the experimental setup that is a short description of gas and silicon detectors and their utility in our experimental apparatus.

- Chapter 3: Includes the data reduction and the transfer reaction cross sections determination.

- Chapter 4: Includes the theoretical analysis of the data in the *DWBA* framework using the code *FRESCO*.

- Chapter 5: Summary and conclusions.

1. Theory

1.1. Direct nuclear reactions

The term, *direct reaction*, characterizes a reaction mechanism which occurs fast and proceeds directly from the initial state to the final without the forming of an intermediate compound state [38]. The time within the incident and the target nucleus interact is very short ($\Delta t \approx 10^{-22}$s) compared to the life time of the corresponding compound nucleus ($t \approx 10^{-17}$s). Therefore, the direct reaction products present different characteristics from the compound ones. The most interesting types of direct reactions are: the *stripping* reaction, its inverse process, the *pick-up* reaction and the *knock-out* reaction.

- "Stripping" reactions

In the case of a stripping (or a pick-up) reaction, when the incident nucleus approaches the target, a strong interaction takes place between the outer nucleons of the projectile and the outer nucleons of the target. Thus, there is a possibility for one or more peripheral nucleons to be detached from the projectile (target) and captured by the target (projectile) (Fig.1a). Assuming a reaction of the form [38]:

$$a + A \rightarrow \underbrace{(a - x)}_{b} + \underbrace{(A + x)}_{B} \qquad (1.1)$$

the Q-value is given by the expression:

$$Q = \left(M_a + M_A - M_b - M_B \right) c^2 \qquad (1.2).$$

The binding energy of nucleus B is:

$$E_B = \left(M_A + M_x - M_B \right) c^2 \qquad (1.3)$$

and the energy separation for the removal of particle x from nucleus *a* is:

$$S_x = \left(M_x + M_b - M_a \right) c^2 \qquad (1.4).$$

Using the formulas (1.3) and (1.4), the final expression for the Q-value of a striping reaction is:

$$Q = -S_x + E_B \qquad (1.5)$$

- ''Pick-up'' reactions

The inverse process of the reaction mechanism described above is known as pick-up reaction. During a peripheral collision between two nuclei, a complex of nucleons (or a single nucleon) is transferred from the target to the projectile (Fig. 1b). Assuming a reaction of the form:

$$a + A \rightarrow \underbrace{(a + x)}_{b} + \underbrace{(A - x)}_{B} \qquad (1.6)$$

the Q-value is evaluated through the expression (1.2).
The binding energy of nucleus b is:

$$E_b = (M_a + M_x - M_b)c^2 \qquad (1.7)$$

and the energy separation for the removal of particle *x* from nucleus *A* is:

$$S_x = (M_x + M_B - M_A)c^2 \qquad (1.8).$$

Using the formulas (1.7) and (1.8), the Q-value of a pick-up reaction is:

$$Q = -S_x + E_b \qquad (1.9).$$

- "Knock-out" reactions

In a knock out reaction [39], one or more nucleons are removed from the target during a high energy collision with the projectile. In a pick-up reaction, one or more ejected nucleons of the target are peaked up by the projectile, while in a knock out reaction since the collision occurs, the ejected particle continues freely (Fig.1c). Assuming the following knock-out reaction:

$$a + A \rightarrow a + x + (A - x) \qquad (1.10)$$

the Q-value is given by the following expression:

$$Q = -S_x \qquad (1.11)$$

where S_x is the energy separation for the removal of particle *x* from nucleus *A*.

These reactions are also known as *quasi-free scattering* because they permit a description of the whole procedure as an interaction between the target and one of the outer nucleons of the projectile (Fig.1c).

Finally, it should be mentioned that in the early stage of the theory, the direct reaction mechanism was treated using a plane wave approximation in which the wave function $\Psi(\mathbf{r})$ can be written as $e^{i\mathbf{k}\mathbf{r}}$. This approximation could not describe properly the reaction process. However, it is well-established now that the incident wave is distorted by the nuclear interaction. Therefore, direct nuclear reactions can give more accurate description when they are treated in the *Distorted Wave Born Approximation* (*DWBA*) framework, the principles of which are given below.
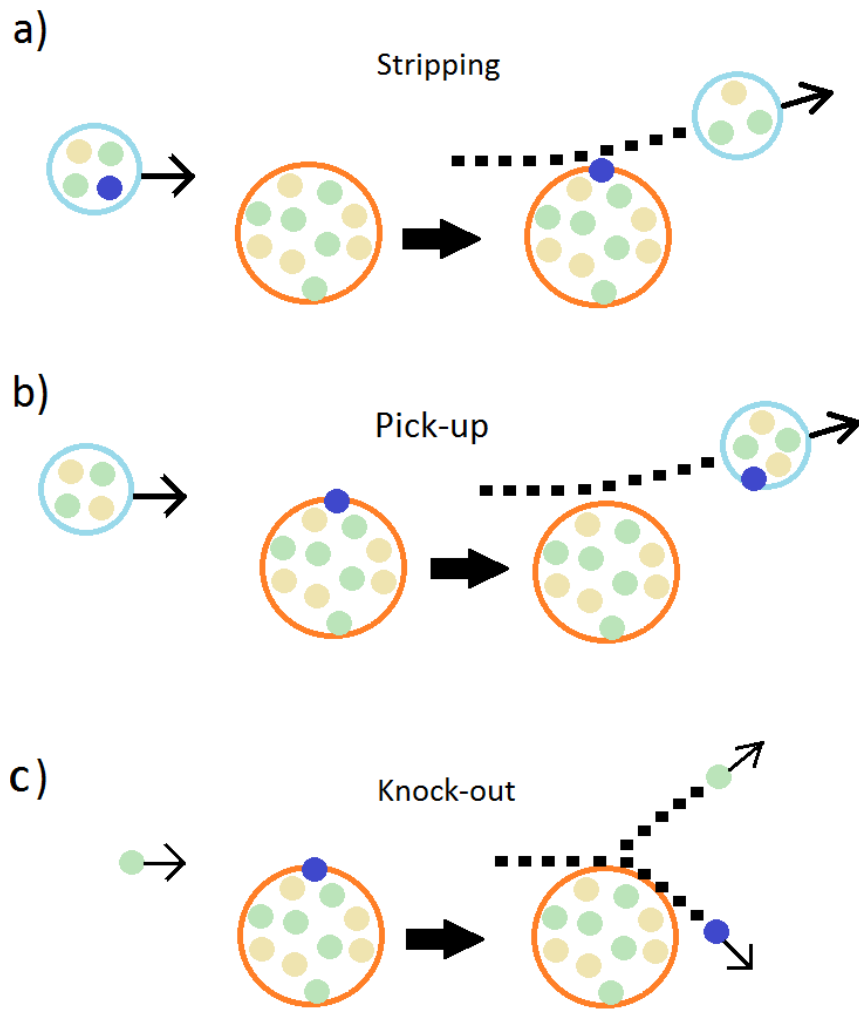
Figure 1*: Schematic representation of direct nuclear reaction mechanisms.*

1.2. Distorted wave Born approximation

In order to describe the scattering by a central force [40], we have to solve a differential equation of the form:

$$\left[-\frac{\hbar^2}{2m}\nabla^2 + V(r) \right]\Psi(r) = E\Psi(r) \qquad (1.12)$$

The solution of the homogeneous equation that corresponds to a plane wave is:

$$\chi_k(r) = A e^{ikr} \qquad (1.13)$$

and so the general solution of Eq.(1.12) is:

$$\Psi_k^{(+)}(r) = e^{ikr} + \int d^3r' G^{(+)}(r,r')V(r')\Psi^{(+)}(r') \qquad (1.14)$$

where

$$G^{(+)}(r,r') = -\left(\frac{2m}{4\pi\hbar^2}\right)\frac{eik|r-r'|}{|r-r'|} \qquad (1.15)$$

is a Green's function and the constant A was set equally to unit. In order to determine the scattering amplitude, we need to know the behavior of $\Psi^{(+)}_k(\mathbf{r})$ for large values of r. The Green's function behaves asymptotically as:

$$G^{(+)}(r,r') \xrightarrow[r\to\infty]{} -\left(\frac{2m}{4\pi\hbar^2}\right)\frac{e^{ikr}}{r}e^{-ik'r'} \qquad (1.16)$$

where the vector **k′** is along **r** and is defined by $k' = k\hat{r}$. So, the wave function defined by Eq. (1.14) has the asymptotic form:

$$\Psi_k^{(+)}(r) \xrightarrow[r\to\infty]{} e^{ikr} - \frac{e^{ikr}}{r}\frac{1}{4\pi}\int d^3r' e^{-ik'r'}U(r')\Psi_k^{(+)}(r') \qquad (1.17).$$

Identifying the scattering amplitude as the coefficient of the outgoing wave, we obtain an integral expression for the scattering amplitude:

$$f(\vartheta,\varphi) = -\frac{1}{4\pi}\int d^3r' e^{-ik'r'}U(r')\Psi_k^{(+)}(r') \qquad (1.18)$$

Despite the simple form of the above equation, we still cannot calculate the scattering amplitude since the integral form contains the unknown wave function $\Psi_k^{(+)}(\mathbf{r'})$, but if the potential $U(\mathbf{r'})$ is weak, the amplitude of $\Psi_k^{(+)}(\mathbf{r'})$ is small and the unknown wave function can be replace by the plane wave $e^{i\mathbf{kr}}$. This is called *First Born Approximation*. That leads to the expression of the scattering amplitude where everything is known:

$$f_{BA}(\vartheta,\varphi) = -\frac{1}{4\pi}\int d^3r' e^{-ik'r'}U(r')e^{ikr'} \qquad (1.19)$$

The scattering amplitude is related to the differential cross section by the well-known formula:

$$\frac{d\sigma}{d\Omega} = |f(\theta, \varphi)|^2 \qquad (1.20)$$

This is a fundamental relation between scattering theory and scattering experiment as it binds the cross section, a purely experimental quantity, with the scattering amplitude which characterizes the wave function at large distances of the target.

Moving one step forward, we can assume that the potential U(**r**) can be written as U(**r**)= U₀(**r**)+U₁(**r**) and for U₀(**r**) the exact solution can be found by solving the equation:

$$\left[-\frac{\hbar^2}{2m} \nabla^2 + U_0(r) \right] x(r) = Ex(r) \qquad (1.21).$$

So, the plane waves of (Eq. 1.13) are replaced with the solutions of the above equation and are called *distorted* waves $x_k^{(\pm)}$(**r**). The $x_k^{(+)}$(**r**) corresponds to a plane wave plus an outgoing scattered wave function while the other one corresponds to a plane wave plus an ingoing scattered wave function. Considering all the above, the asymptotic form of the $\Psi_k^{(+)}$(**r**) is:

$$\Psi_k^{(+)}(r) = x_k^{(+)}(r) - \frac{e^{ikr}}{r} \frac{1}{4\pi} \int d^3r' x_{k'}^{(-)*}(r') U_1(r) \Psi_k^{(+)}(r') \quad (1.22)$$

If U₁(**r**) is sufficiently weak compared to U₀(**r**), $\Psi_k^{(+)}$(**r**′) can be replaced by $x_k^{(+)}$(**r**). This is called *Distorted Wave Born Approximation* and leads to the expression for the scattering amplitude:

$$f_{DWBA}(\theta, \varphi) = f_0(\theta, \varphi) - \frac{1}{4\pi} \int d^3r' x_{k'}^{(-)*}(r') U_1(r') x_k^{(+)}(r') \quad (1.23)$$

The entire above are referred to the elastic scattering process. We can generalize the whole procedure for the case of rearrangement reactions. Then, the potential U₀(**r**) is chosen to describe the elastic scattering process while U₁(**r**) describes the interaction that corresponds to the rearrangement reaction. As a result, it is valid to use *DWBA* if only the elastic scattering is stronger than any other possible process. Then, the scattering amplitude for the reaction A(a,b)B has the form of:

$$f_{DWBA}(\theta, \varphi) = -\frac{1}{4\pi} \int\int dr_\alpha dr_\beta x_{k\beta}(r_\beta)^{(-)*} \langle b, B|U_1|a, A\rangle x_{ka}^{(+)}(r_a) (1.24)$$

where instead of x_k (Eq. 1.23), we have $x_{k\alpha}$ and $x_{k\beta}$. The first one is used to describe the elastic scattering at the entrance channel (α= a+A), while the second one is used to describe the elastic scattering at the output channel (β= b+B).

In the present work, the transition amplitudes for the transfer reactions were evaluated in the *DWBA* approximation. The relevant steps described above were performed using the code *FRESCO* [41], details of which are presented on the Appendix I. It should be mentioned that, the transfer amplitudes present strong

dependence from the projectile-target interaction. This interaction can be described in the *Optical Model* framework details of which are presented in the following session.

1.3. Optical model

In the optical model framework the interaction between two nuclei is represented by a complex potential. Both real and imaginary parts of the complex potential are energy dependent. The real part is referred to the refraction while the imaginary part accounts for the loss of flux in the elastic channel [41]. The imaginary part of the potential interacts with the incident wave and attenuates it [38]. At low energies, it is expected that this attenuation is dominant near the nuclear surface, but as the bombarding energy increases, the absorption of the incident wave may take place throughout the whole volume of the nucleus. So, in the optical model analysis, both surface and volume absorption terms are adopted.

In the optical model framework, both *microscopic* and *macroscopic* potentials are invoked. In the microscopic approach the real part of the potential is obtained by assuming a nucleon-nucleon effective interaction. In contrast, the macroscopic description does not treat the nucleus as a system of different nucleons and thus, the interaction between the projectile and a target can be described in terms of a *mean potential*.

In the present work, the results were analyzed in a macroscopic framework adopting the *LC* and the *Christensen* potential, as well as in microscopic framework where the *BDM3Y* interaction was adopted. Some details of these potentials are given below, while the results of the analysis will be discussed on chapter 4.

1.3.1. Macroscopic approach

In the macroscopic approach the simplest form of both the real and imaginary parts are described by a *square well* potential [38] given by the following expression:

$$V(r) = -(V_0 + iW_0) \tag{1.25}$$

where V_0 and W_0 are the depths of the real and the imaginary part respectively. However, such a potential does not accurately describe any the elastic scattering data.

The most famous macroscopic potential however, was proposed by Woods and Saxon [42], and replaces the square well by a smoother one giving cross sections with better agreement with experimental results. The assumed form of this potential is:

$$V(r) = -\frac{V_0}{1 + e^{[(r-R)/a]}} \tag{1.26}$$

where R is measure of nuclear size and a determines the diffuseness of the nuclear surface. A comparison between these two potentials is presented in Figure 2. It is

obvious that for large values of r, the potential drops to zero, reflecting the short-range character of nuclear forces. It should be mentioned here that in general, the optical model analysis yields better fits to the experimental data when an additional term, like the *Spin-Orbit* term [43], is added to the volume term.
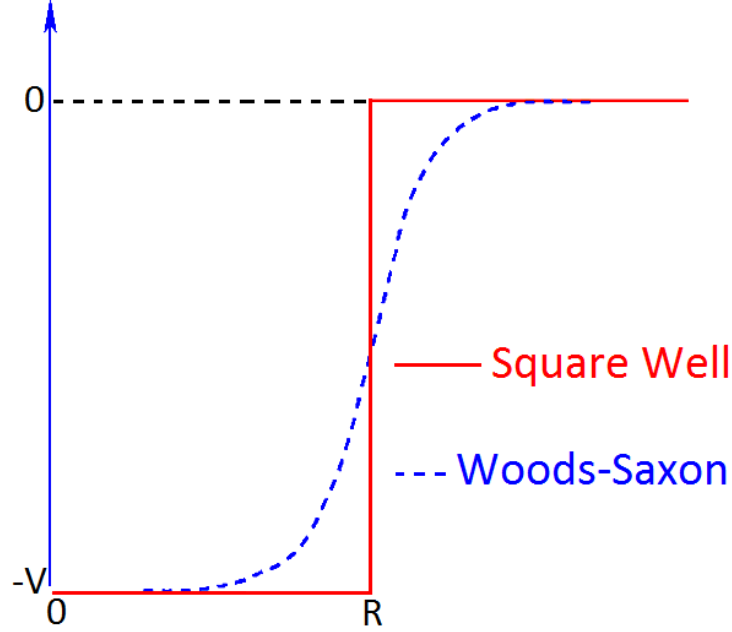
***Figure 2**: Comparison between the square-well and the Woods-Saxon potential.*

Another point that we would like to stress out here is the well known problem of potential ambiguities. In this, different families of potentials can provide equivalent fits to the data. These families cross each other at a specific radial point *x*. In the vicinity of this point the nuclear potential can be well and uniquely determined. Based on that, P. R. Christensen and A. Winther [44] performed a comparison between different expressions for ion-ion potentials and the experimental values *V(r)* deduced from various heavy ion (*HI*) collisions, in order to determine the real part of a global nuclear potential. As a result, a macroscopic description that seems to interpret the real part of the nuclear potential for various *HI* systems is:

$$U_N(r) = 50 \frac{R_P R_T}{R_P + R_T} e^{-\frac{r - R_P - R_T}{a}} \qquad (1.27)$$

where the radius of both projectile (R_P) and the target (R_T) is calculated through the expression:

$$R_i = 1.233 A_i^{1/3} - 0.978 A_i^{1/3}, i = P, T \qquad (1.28)$$

and the diffuseness parameter *a* was fixed at 0.63fm.

A comparison between this potential and the potentials deduced from experimental data is illustrated in Figure 3. It is shown that in the energy range of E_{lab}= (11-100) MeV for light projectiles ($5 \leq Z \leq 10$) and various targets ($5 \leq Z \leq 83$), the variation between these potentials is small. For systems close to ours ($A_P^{1/3} + A_T^{1/3} \approx$

5.80), the ratio $V(x)/U_N(x)$ is almost one indicating that this empirical potential can provide reasonable predictions to cross sections.
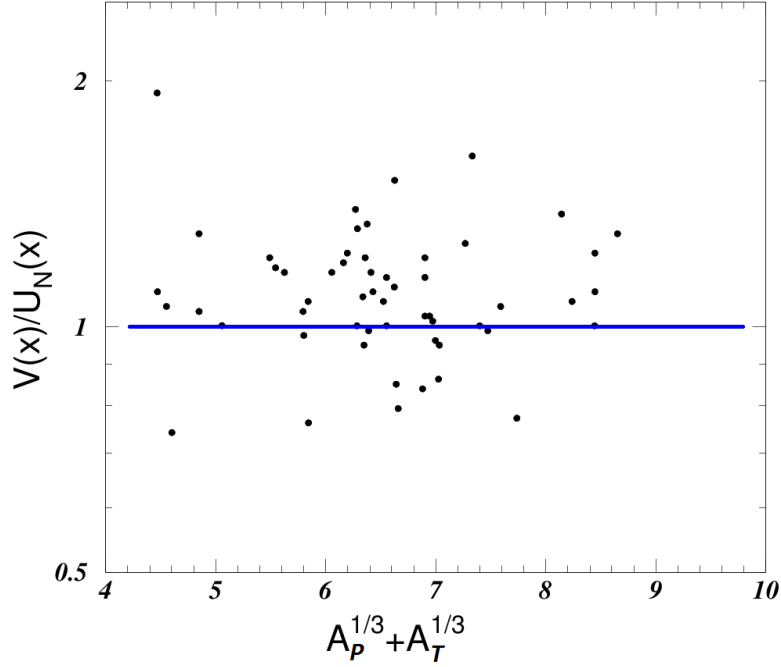
Figure 3*: A comparison between the empirical potential U_N and the experimental values V in the crossing point **x** for various HI systems.*

However, it has to be noted that for systems similar to ours, like $^{16}O+^{28}Si$ [45,46] or $^{12}C+^{24}Mg$ [47], where both projectile and target present cluster structure, the optical model analysis discussed above fails to reproduce the data sufficiently well especially at the more backward angles. Thus, in order to describe such unusual angular distributions where oscillation pattern occurs, several potentials like Ginocchio potential in [48], Kobos-Satchler potential [49] or the Lee Chan potential (*LC*) were invoked.

Especially, for the system $^{16}O+^{28}Si$, S. K. Agarwalla et al. performed an optical model analysis in a wide energy range [50], using the *LC* potential [51]. It was found that the *LC* potential provided reasonable fits to the data in the energy range of E_{lab}= (50-55) MeV, by reproducing the back angles oscillations. Some details of this potential are given below.

The *LC* potential consists of a *Woods-Saxon* (WS) potential plus an additional term:

$$V(r) = -(V_0 + iW_0)\left[1 + e^{[(r-R)/b]} + \beta e^{[(r-R)/a]}\right]^{-1} \qquad (1.29)$$

This additional term is of great importance at small distances in the interior. On the other hand, for large values of r, the additional term becomes less significant and the *LC* potential presents the same behavior as a *WS* potential does.
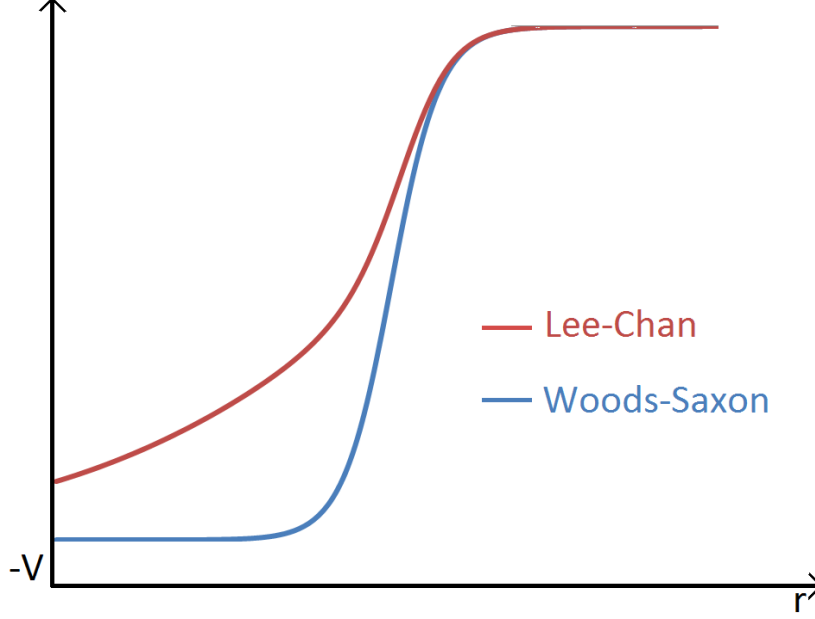
_Figure 4__: Comparison between Woods-Saxon and Lee-Chan potential._

1.3.2. Microscopic approach

The microscopic heavy-ion scattering potential of interest is obtained in a double folding model, by using an effective nucleon-nucleon (NN) interaction folded over matter densities of the interacting nuclei [52]. For composite projectiles that interact with a target nucleus, the overall potential can be written as:

$$U\left(\vec{R}\right)=\int d\vec{r_1}\int d\vec{r_2}\rho_P\left(\vec{r_1}\right)\rho_T\left(\vec{r_2}\right)u\left(\vec{r_{12}}\right) \tag{1.30}$$

where $\rho_i(r)$, $i=P,T$, are the density distributions of the projectile and the target respectively, R is the distance between the center of mass of the colliding nuclei and u is the effective NN interaction. In principle, the effective interaction has the form:

$$u\left(r_{12}\right)=u_{00}+u_{01}\tau_1\cdot\tau_2+u_{10}\sigma_1\cdot\sigma_2+u_{11}\sigma_1\cdot\sigma_2\tau_1\cdot\tau_2 \tag{1.31}$$

where $\boldsymbol{\sigma}$ and $\boldsymbol{\tau}$ are the Pauli matrices for spin and isospin respectively.

The *M3Y* effective interaction is the oldest and the most popular interaction which is widely and successfully used in elastic scattering and other reactions. For the elastic scattering of spinless particles (like ^{20}Ne and ^{28}Si), only the first term of Eq.1.31 contributes to the overall potential. That leads to a simpler form for the M3Y interaction:

$$u\left(r_{12}\right)=u_{00}\left(r\right) \tag{1.32}$$

where

$$u_{00}\left(r\right)=\left[7999\frac{e^{-4r}}{4r}-2134\frac{e^{-2.5r}}{2.5r}\right]MeV \tag{1.33}$$
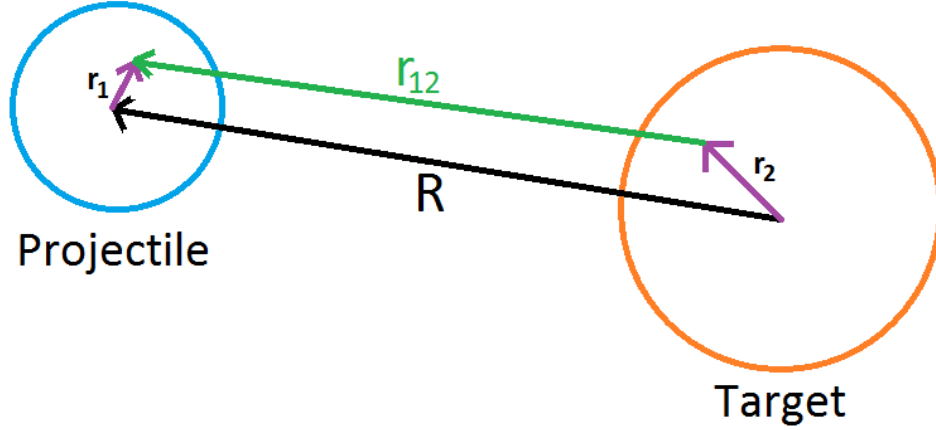
Figure 5*: Surface integral coordinates.*

It is well-established, that the wave function of *N* identical fermions has to be antisymmetric. However, the term that describes the effective interaction between two nearby nucleons in the same nucleus is not antisymmetric. To correct that, an additional correction term was added to the above relation and the overall effective interaction is given by the expression:

$$u_{00}(r) = \left[7999 \frac{e^{-4r}}{4r} - 2134 \frac{e^{-2.5r}}{2.5r} - 276 \left(1 - 0.005 \frac{E}{A} \right) \delta(r) \right] MeV \quad (1.34).$$

It should be noted that the M3Y interaction is density independent. Therefore, it is used only in a short density range approximately the 1/3 of the density of a normal nuclear matter. In a more realistic analysis, it is necessary to include a density dependent interaction, like the following:

$$u_{00}^{DD}(r, \rho, E) = f(\rho, E) u_{00}(r) \qquad (1.35)$$

where u_{00} is the original *M3Y* interaction. The function *f (ρ,E)* can be parameterized in the following form:

$$f(\rho, E) = C(E) \left[1 + a(E) e^{-\beta(E)\rho} \right] \qquad (1.36)$$

where ρ is the density of nuclear matter and *C(E)*, *α(E)* and *β(E)* are energy dependent parameters. This interaction is known as *DDM3Y* interaction (Density Dependent M3Y).

The following form of the *f (ρ,E)* was introduced by Myers et al. [53,54].

$$f(\rho) = C \left[1 - a\rho^{\beta} \right] \qquad (1.37)$$

This is called *BDM3Y* interaction and into this context, the overall potential can be written as:

$$U(\vec{R}) = \int d\vec{r}_1 \int d\vec{r}_2 \rho_P(\vec{r}_1) \rho_T(\vec{r}_2) u_{00}(r) \left[C \left(1 - a\rho^{\beta} \right) \right] \qquad (1.38).$$

Some typical parameters for different types of *BDM3Y* interaction are presented in Table 1.

Table 1: *Typical parameters for the different types of BDM3Y interaction.*

Interaction	C	a	β
BDM3Y0	13.827	1.1135 fm^2	2/3
BDM3Y1	12.253	1.5124 fm^3	1.0
BDM3Y2	10.678	5.1069 fm^6	2.0
BDM3Y3	10.153	21.073 fm^9	3.0

It is necessary to mention that the microscopic interactions described above are purely real and so, the imaginary part of the optical potential has to be treated phenomenological.

2. Experimental setup

2.1. The ICARE chamber

The measurements were performed at ICARE target facility at the Heavy Ion Laboratory of the University of Warsaw, using a ^{20}Ne beam and a ^{28}Si target mounted on a rotating target system. The ICARE system consists of a large, one meter diameter reaction chamber, with two rotating platforms (A and B) and several rings, for allowing the setup of numerous detectors as appear in Figure 6. In this experiment, both silicon and gas detectors were used. Therefore, some general characteristics of their function are presented in the following chapter.
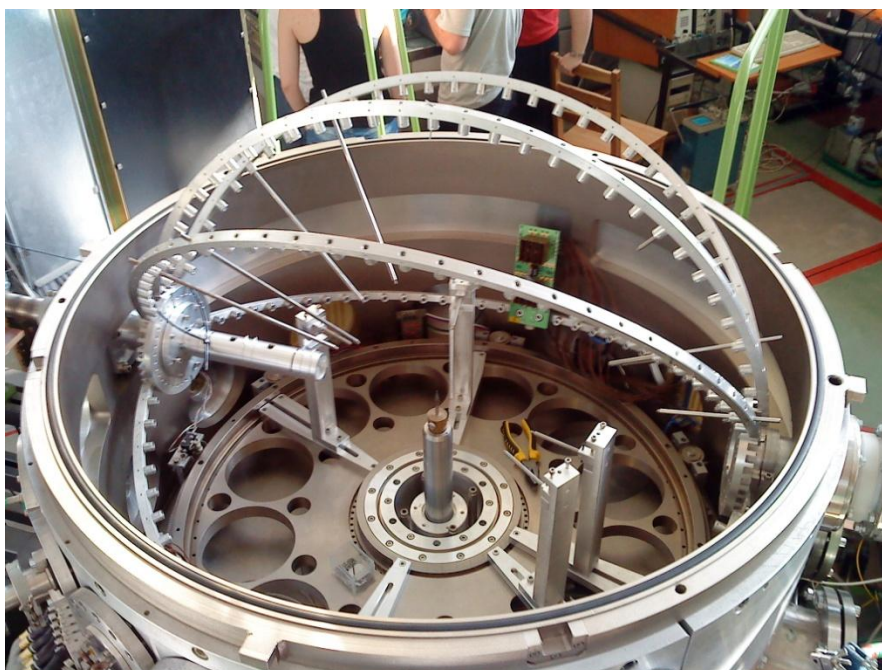
Figure 6*: ICARE chamber.*

Inside the ICARE chamber, a motherboard is attached, which includes the preamplifiers. The motherboard is shown in Figure 7. After this stage, the analog and logic signals are fed to the appropriate electronics (amplifiers, discriminators and ADC's) to be modified properly and finally to be handled by the acquisition system named as Midas. The same program provides a facility for handling the performance for all electronics and power supplies.
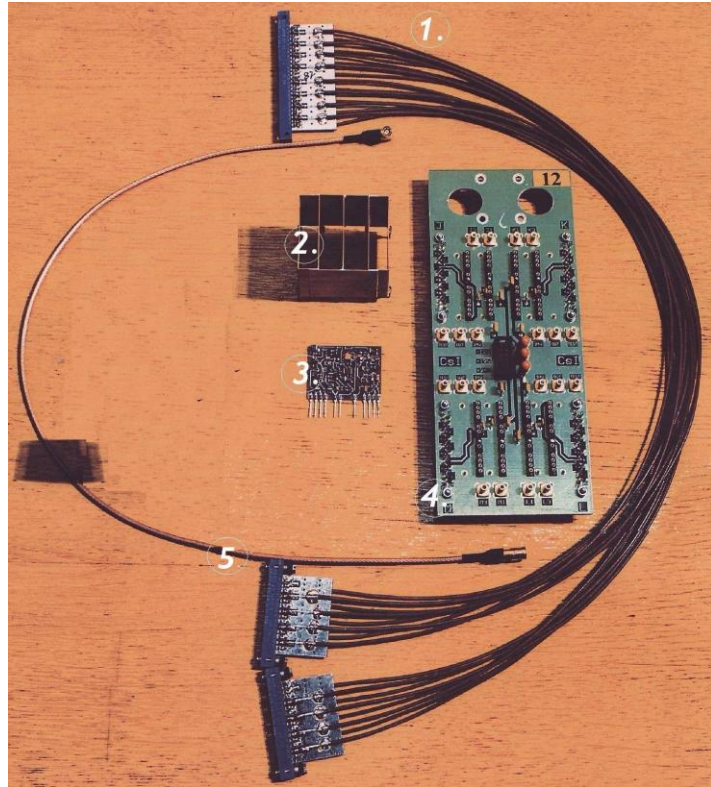
Figure 7: The ICARE electronics. 1: Motherboard cable, 2: Preamplifier cover, 3: Preamplifier, 4: Motherboard and 5: Detector voltage supply cable.

2.2. Silicon detectors

The Si detector function is based on the properties of a *p-n junction*. A p-n junction in a semiconductor is the border plane between a p-type zone, doped with electron-acceptor impurities, and a n-type zone doped with electron-donor impurities [55]. A p-n junction consists of a weakly doped p-silicon into which a layer of n-type impurities is introduced. At the boundary between the two types of material a double layer of charges is formed in the following way: conduction electrons from the n-side move towards the p-side material while holes diffuse across the junction into the n-type zone. As a result, the diffusion of conduction electrons out of the n-type material leaves behind positive charges in the form of ionized donor impurities. At the same time, each hole that is removed from the p-side of the junction leaves behind an acceptor site that has picked up an extra electron [56]. The built up of this double layer is slowed down by the electric field produced by the space charges until the equilibrium is reached (Fig.8). At equilibrium, that steady electric filed prevents further diffusion across the junction. The layer over which the charge imbalance exists is called the *depletion region*.

In the present setup, *surface barrier silicon detectors* were used to measure the energy loss of the incident ions. The depletion region in such a detector is formed

throughout the whole semiconductor (fully depleted detector). When a charge particle passes through the depletion region, a part of its energy is deposited at the detector and thus, equal number of electrons and holes is generated along the particle track. Then, with an electric field present throughout the active volume of the detector, both charged carriers feel the electrostatic forces that cause them to move in opposite directions. The charge which is collected by the electrodes is proportional to the energy deposition and thus, the output pulse height is proportional to the energy loss of the ion.
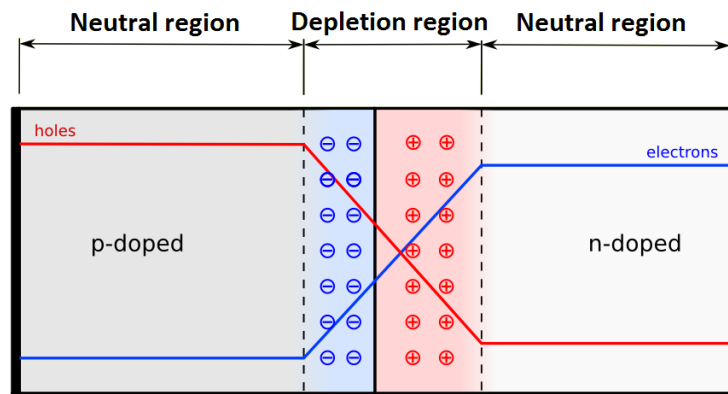
_Figure 8__: Schematic representation of a p-n junction at equilibrium._

2.3. Gas detectors

Gas detectors function is based on the collection of the ionization events produced in gas by passing radiation. The basic configuration of such a detector consists of a container filled with an appropriate gas. The container has conducting walls and a thin window [57]. Considering a cylindrical container for simplicity, a conducting wire (anode) is placed along its axis (Fig.9).
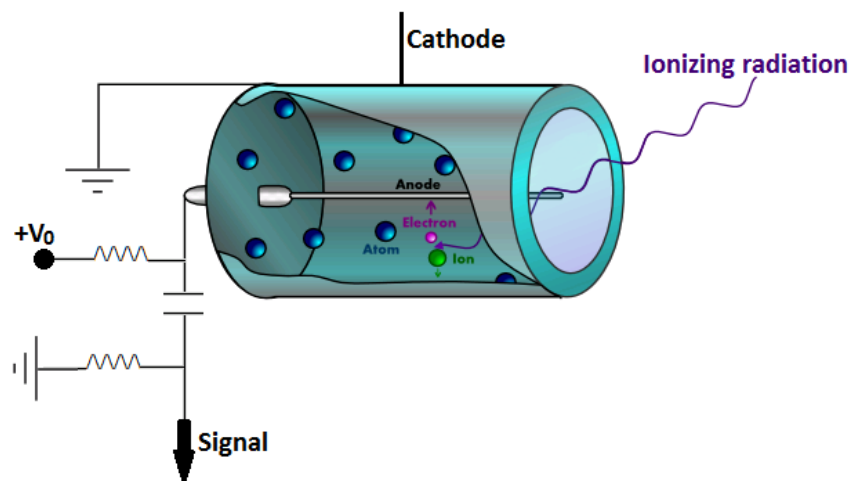
_Figure 9__: Basic construction of a simple gas ionization chamber._

As a result, a radial electric field is persistent. When radiation passes through the detector, a number of electrons and ions is formed along its track. The mean number of the pairs is proportional to the incident radiation energy. Then, with the presence of the electric field, the electrons and the ions are forced to move towards the anode and the cathode respectively.

It should be mentioned that the charge which is collected by the anode (or the cathode) depends on the applied bias. By increasing the voltage, the number of the collected ions raises and based on that, four discrete regions can be distinguished: The *recombination*, the *ionization*, the *proportional counter* and the *Geiger-Müller* region (Fig.10).

In the first region, the number of collected ions is small as the coulomb attraction is strong enough leading to electron-ion recombination. Then, as the voltage is raising the coulomb forces are overcome and thus, a greater number of electrons and ions are collected. In the third stage, with the presence of a strong electric field, free electrons are accelerated and through collisions with the gas atoms, secondary ionizations take place and so on. However, the number of ion-electron pairs is proportional to the primary number of electrons leading to a proportional amplification of the signal.
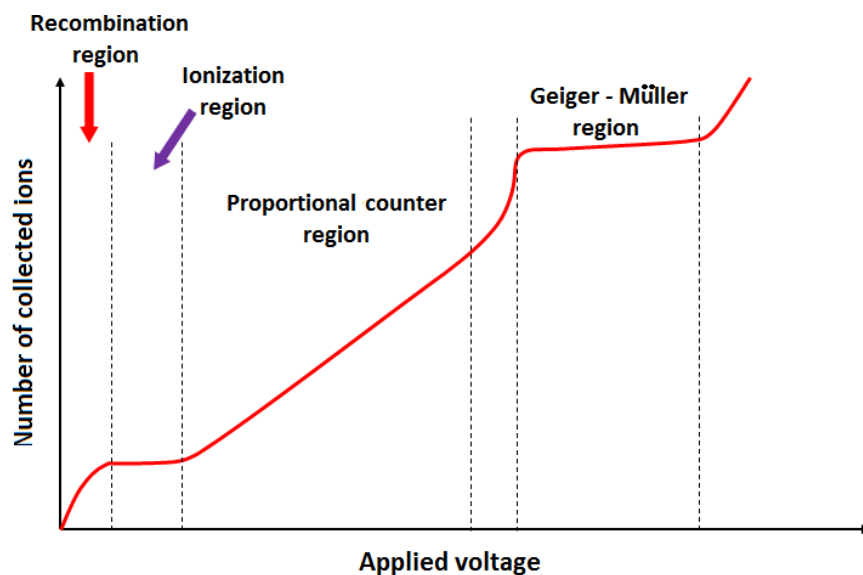
Figure 10: *Number of collected ions by a gas detector as a function of the applied voltage where for discrete regions can be distinguished: The recombination, the ionization, the proportional counter and the Geiger-Müller region.*

Finally, in the last region due to the high voltage the number of ionization events is very large leading to signal saturation and so, the "information" about the incident radiation energy is lost. The detectors working in that region are called *counters* as they provide information only about the number of the incident particles.

Taking into account all the above, in our experiment the gas detectors were used as ionization chambers. This region is preferable as the number of collected ions is almost constant, preventing serious variations due to voltage shift.

2.4. Detectors – Telescopes

In this experiment both silicon detectors and telescopes were used. The telescopes, consisting of a gas detector followed by a 500 μm thick Si detector, have provided identification of the produced particles via a ΔE-E technique. The telescope window is a Mylar foil 2.5 μm thick and the gas detector, 47 mm thick, is filled with isobutene at a pressure of 15 mb. At the backward angles where the energy of the particles is expected to be low, Si detectors 40μm thick were used [58].

In order to define in a more accurate way their solid angle, masks were placed in front of all the detectors and telescopes. The mask dimensions for the telescopes were (3.5x10.5) mm, for the single detectors (4x7) mm while for the two monitors (2x7) mm. More details about the structure of a telescope and a silicon detector are shown in Figure 11 and 12 respectively.
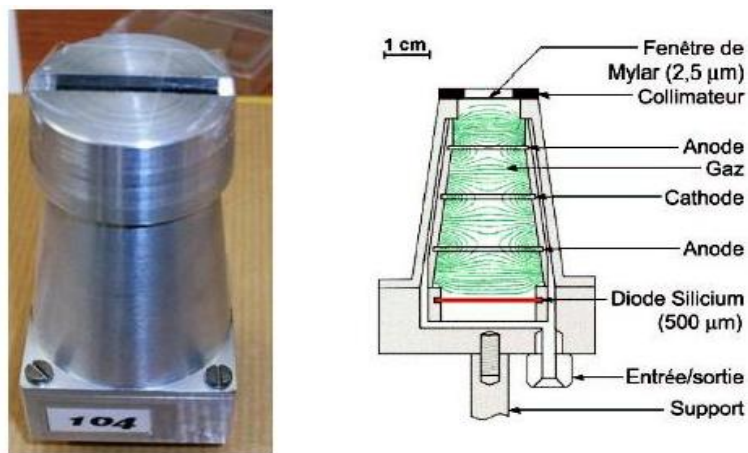
Figure 11*: Telescope structure.*
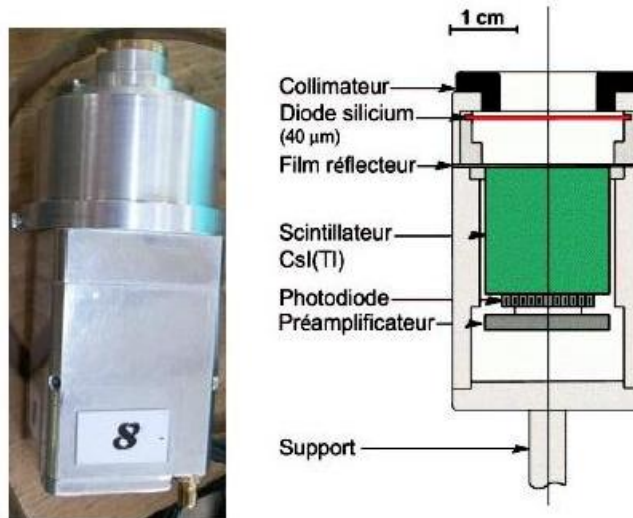
Figure 12*: The Si detector structure.*

2.5. Details of the setup

2.5.1. Detectors' position

As it was mentioned, ICARE chamber has various facilities for setting up numerous detectors. In this respect, the chamber includes two platform and several rings. Taking into account preliminary calculations for elastic scattering and transfer reactions, detectors and telescopes were chosen to be placed according to the following lay out.

Platform A: In this platform a telescope (T1) and a silicon detector (S1) were placed in an angular distance of 50° between them. So, the rotating platform was set to span the angular range between $\theta_{lab}=25^o$ and $\theta_{lab}=135^o$ in steps of 5° corresponding to 36° and 154° in the center of mass respectively.

Platform B: In this platform a telescope (T2) was set to span the angular range between $\theta_{lab}=37^o$ and $\theta_{lab}=60^o$ while, another telescope (T3) was set to rotate between $\theta_{lab}=57^o$ and $\theta_{lab}=80^o$.

Rings: Eight single detectors were placed fixed at the rings. Two monitors (M1,M2) were mounted at symmetrical forward positions for normalization purposes and correcting possible beam misalignments. Also six more detectors were fixed at $\theta_{lab}=45^o$, 55°, 75°, 85°, 100°, and 125° as the cross section there is expected to be low. Some details of the experimental setup are presented in Table 2.

It should be noted however that the main tool in our analysis was the two stage telescopes where, the ΔE-E technique, allowed a good discrimination between the reaction events and the obtained spectra were adequately clear.
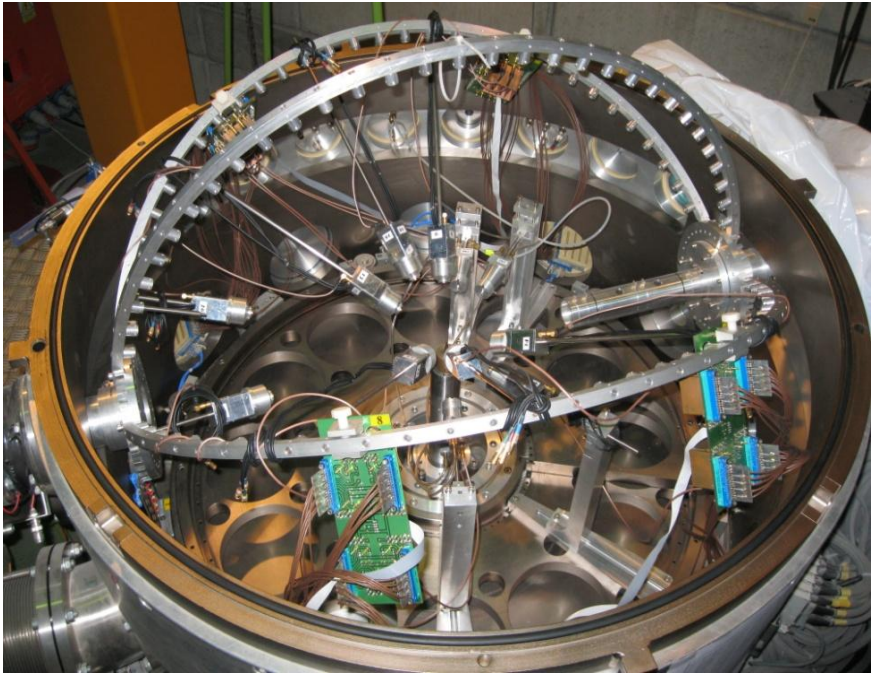
Figure 13*: ICARE chamber with the present setup.*
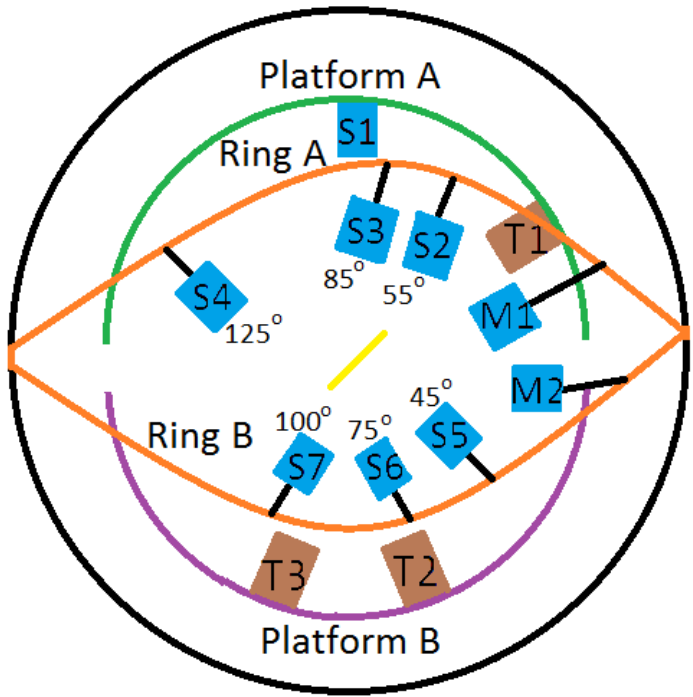
Figure 14*: Schematic details of the setup.*

Table 2: *Detectors' distances from the target.*

Detector Name	Detector ID	Distance from the target (cm)
M1	8	31.5
M2	26	31.5
T1	104	11.5
T2	106	11.5
T3	107	11.5
S1	19	11.4
S2	11	11.1
S3	23	11.5
S4	24	11.5
S5	13	11.6
S6	16	13.5
S7	9	11.6

2.5.2. Targets' position

At the middle of the chamber a target ladder was placed with several available positions. An alpha source was mounted at the first target position for the energy calibration, one was kept blank and apart from the ^{28}Si targets, a gold target was also mounted for defining the beam energy and quartz for defining beam position. A photo of the target holder with some details of targets is presented in Figure 15.

Figure 15: *Target holder*

3. Data reduction

3.1. Energy calibration

In order to identify the different reaction products, a precise energy calibration is essential. Energy calibration for each detector was performed via a ^{241}Am source and a pulser. The pulser was calibrated through the alpha source (Fig.16) and the detectors via the pulser in a wide energy range (Fig.17). More details about calibration process are presented on the Appendix V.
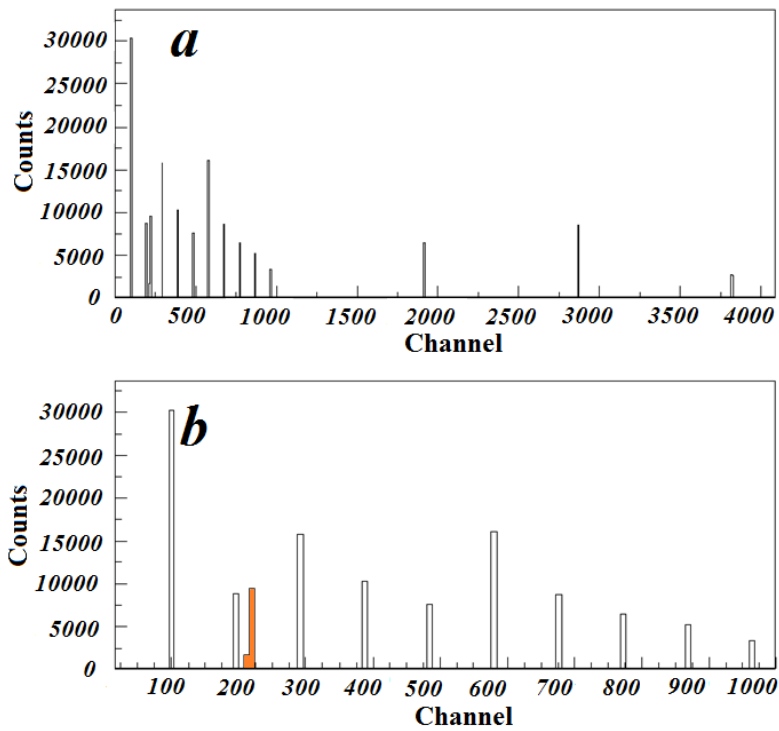
Figure 16: *a) A pulser spectrum for the telescope T1-E. b) An expanded pulser spectrum where the alpha peak is denoted with the orange color.*
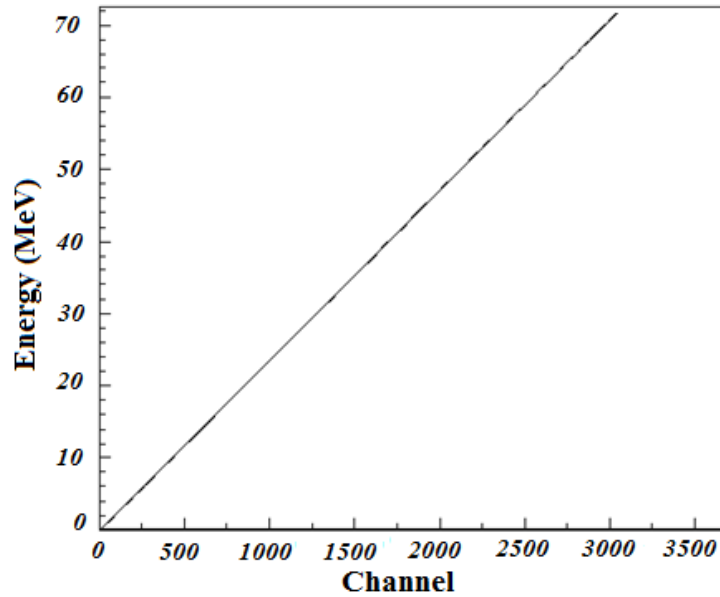
Figure 17: *Energy calibration for telescope T1-E in a wide energy range.*

3.2. Identification of reaction channels

In the present work, we study transfer reactions for the system ^{20}Ne+^{28}Si at near barrier energies. Particle identification was required to separate the different reaction products and that was achieved by the standard ΔE-E technique. A typical two dimension spectrum is shown in Figure 18, where the different contours are well-formed. The analysis of the data was performed using the program *PAW* [59]. Taking into account the kinematics of the colliding ions and the energy loss, using the *NRV* [60] and the program *LISE++* [61] respectively, the identification of the different reaction channels was performed as appear in Table 3. It is obvious that for the different contours additionally to the main entrance channel **^{20}Ne+^{28}Si**, some other reaction channels are also observed due to target contaminations.

In the ^{24}Mg contour, the pick-up reaction products [**^{28}Si (^{20}Ne, ^{24}Mg) ^{24}Mg**] are denoted with the red circle, but as it was mentioned, additional reaction products were also observed. Taking a projection on E axis (Fig.19), some other peaks are also pronounced. In particular, due to target oxidation the reaction channel [**^{16}O (^{20}Ne, ^{24}Mg) ^{12}C**] was observed around channel 500, while another peak is appeared around channel 800 due to ^{24}Mg contamination in the target. The peak of interest, denoted with the red arrow, is well pronounced but the statistics is low. This is a result of the low cross section that characterizes the specific reaction channel combined with the low current intensity which was fluctuated between 0.5 and 1.0 electrical nA.

Table 3: *A list of the observed reaction channels.*

Contour	Reaction	Q-value (MeV)
^{24}Mg	^{24}Mg(^{20}Ne,^{24}Mg)^{20}Ne	0.000
	^{28}Si(^{20}Ne,^{24}Mg)^{24}Mg	-0.670
	^{16}O(^{20}Ne,^{24}Mg)^{12}C	2.150
^{20}Ne	^{28}Si(^{20}Ne,^{20}Ne)^{28}Si	0.000
	^{16}O(^{20}Ne,^{20}Ne)^{16}O	0.000
	^{24}Mg(^{20}Ne,^{16}O)^{28}Si	5.250
^{16}O	^{16}O(^{20}Ne,^{16}O)^{20}Ne	0.000
	^{28}Si(^{20}Ne,^{16}O)^{32}S	2.220
^{12}C	^{12}C(^{20}Ne,^{12}C)^{20}Ne	0.000
	^{28}Si(^{20}Ne,^{12}C)^{36}Ar	1.700
	^{16}O(^{20}Ne,^{12}C)^{24}Mg	2.150
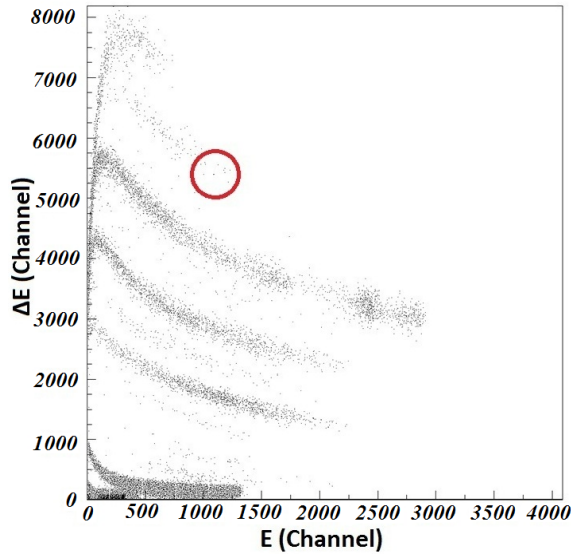
Figure 18: *A typical 2-d spectrum for telescope T1 at θ_{lab}= 45°, E_{lab}=70 MeV. Particle identification was performed via the ΔE-E technique, where the pick-up reaction products are denoted with the red circle.*
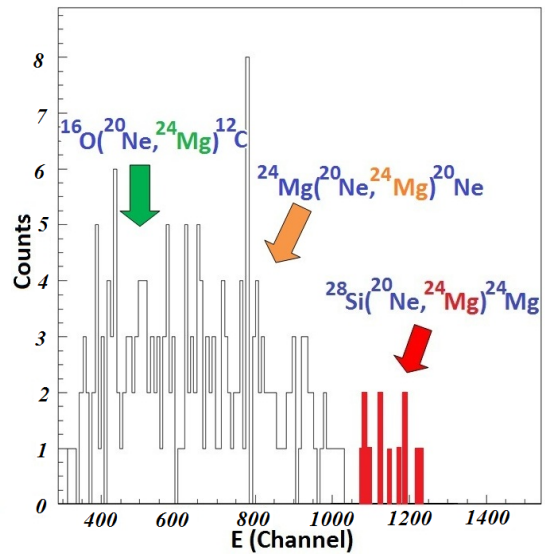
Figure 19: *The projection of ^{24}Mg contour on E axis for telescope T1 at θ_{lab}= 45°, E_{lab}=70 MeV.*

In the ^{16}O contour, the one-alpha transfer products of the main reaction channel are denoted with the green circle (Fig.20), where an alpha particle is transferred from the projectile to the target (stripping reaction). Taking a projection on E axis (Fig.21), other peaks are also pronounced, identified as oxygen from the elastic scattering ^{16}O (^{20}Ne, ^{16}O) ^{20}Ne and the reaction ^{24}Mg (^{20}Ne, ^{16}O) ^{28}Si on contaminants ^{16}O and ^{24}Mg respectively.

Finally, we identified ^{12}C nuclei due to the week reaction channel ^{28}Si (^{20}Ne, ^{12}C) ^{36}Ar. A two dimension spectrum is presented in Figure 22, where the transfer products are denoted with the black circle. The cross section for the specific reaction is expected to be low (~0.1mb) which is reflected on a poor number of counts in the peak. Looking at the single spectrum (Fig.23), although the peak is well pronounced it barely consists of 20 counts with a bad impact on the statistical error. Other pronounced peaks are also observed due to target contaminations.
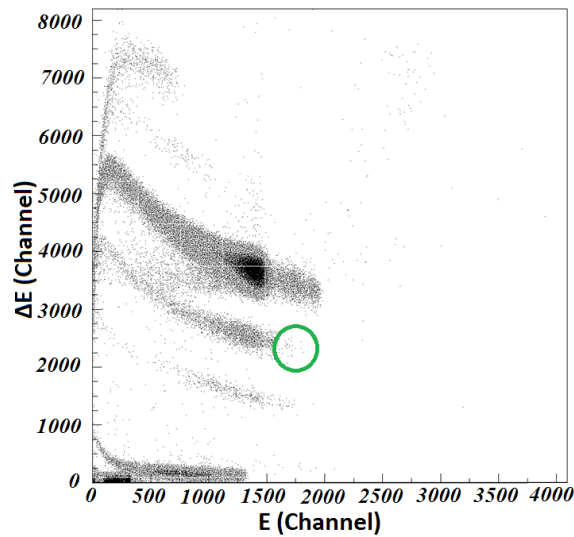
Figure20: _A typical 2-d spectrum for telescope T1 at θ_{lab}= 33°, E_{lab}=52.3 MeV. Particle identification was performed via the ΔE-E technique, where the one-alpha transfer products are denoted with the green circle._
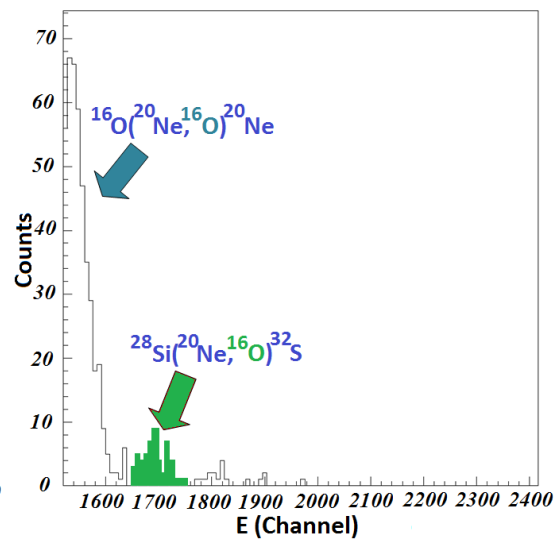
Figure 21: _The projection of ^{16}O contour on E axis for telescope T1 at θ_{lab}= 33°, E_{lab}=52.3 MeV._
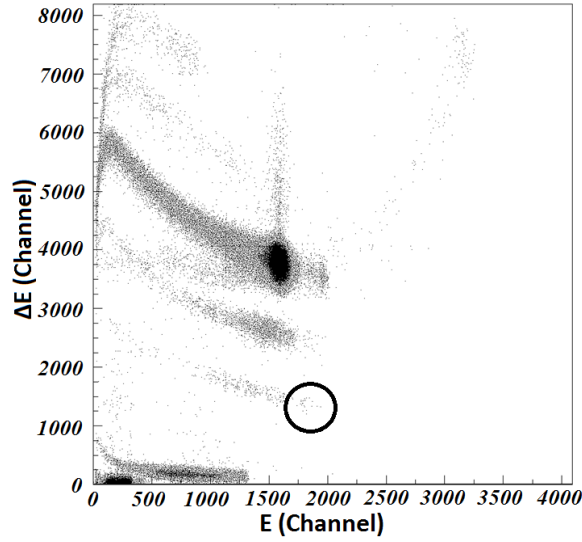
Figure 22: *A typical 2-d spectrum for telescope T1 at $\theta_{lab}= 30^o$, $E_{lab}=52.3$ MeV. Particle identification was performed via the ΔE-E technique, where the one ^8Be transfer products are denoted with the black circle.*
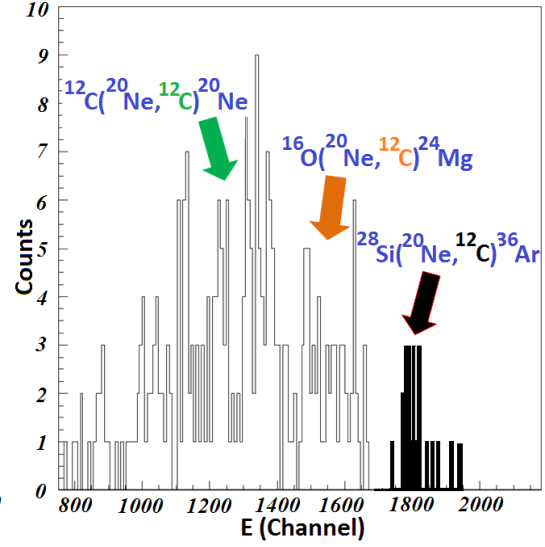
Figure 23: *The projection of ^{12}C contour on E axis for telescope T1 at $\theta_{lab}= 30^o$,*

3.3. Determination of cross sections

The cross section gives us the probability for a reaction to take place. For the transfer reactions mentioned above, the cross section was evaluated through the expression:

$$\sigma(\theta) = \frac{N}{(D\Phi)\Omega} \qquad (3.1)$$

where:

N is the number of counts,

D represents the scattering centers,

Φ is the flux of the beam and

Ω is the solid angle of the detector.

The ($D\Phi$) quantity was calculated via elastic scattering information. At $\pm 20^o$ where the two monitors were placed, we have pure Rutherford scattering and thus, the ($D\Phi$) is given by the expression:

$$(D\Phi) = \frac{N_m}{\sigma_{Ruth}\Omega_m} \qquad (3.2)$$

where:

N_m is the number of counts of the monitor,

σ_{Ruth} is the Rutherford scattering cross section and

Ω_m is the solid angle of the monitor.

Using the formulas (3.1) and (3.2), the final expression for the cross section is:

$$\sigma(\theta) = \frac{N}{\Omega}\frac{\sigma_{Ruth}\Omega_m}{N_m} \qquad\qquad (3.3)$$

As a result, the cross section is evaluated through a simpler and more accurate expression which does not depend on scattering centers and therefore from the target thickness or the flux of the beam.

      The Rutherford scattering cross section was calculated using the program *LISE++* while, the solid angle for each detector was calculated by the known activity of ^{241}Am source as:

$$\Omega = 4\pi\frac{N_a}{Rt} \qquad\qquad (3.4)$$

where:

N_a is the number of counts of the alpha peak,

R is the activity of the source (40 kBq) and

t is the record time.

      The solid angle was also calculated by the program *GATE* [62,63]. *GATE* is a simulation toolkit based on *Geant4 Monte Carlo* simulation, details of which are presented on the Appendix II. In our simulation, a cylindrical isotropic alpha source (^{241}Am) with radioactivity 40kBq was used. The geometry of ICARE detecting system was introduced in *GATE* as it is presented in Table 4. Also, a comparison of the simulated and experimental values of the solid angle used in the experimental analysis is included in Table 5.

      Although the variation between the experimental and the simulated solid angle values is significant, at the cross section calculation Eq. (3.3), the ratio Ω_m/Ω is introduced. Therefore, the actual variation between the experimental and the simulated Ω_m/Ω ratio is presented in Table 6.

Table 4: *The Geometry of the Monte Carlo simulation.*

Detector	Distance from the source (cm)	Mask (mm²)	Thickness of the detector	Radius of the source (mm)	Thickness of the source (mm)
M1	31.5	2x7	40μm	1.5	0.1
M2	31.5	2x7	40μm	1.5	0.1
T1-gas	11.5	3.5x10.5	47 mm	1.5	0.1
T2-gas	11.5	3.5x10.5	47 mm	1.5	0.1
T3-gas	11.4	3.5x10.5	47 mm	1.5	0.1
T1-Si	17.1	3.5x10.5	500μm	1.5	0.1
T2-Si	17.1	3.5x10.5	500μm	1.5	0.1
T3-Si	17.0	3.5x10.5	500μm	1.5	0.1
S3	11.5	4x7	40μm	1.5	0.1
S4	11.5	4x7	40μm	1.5	0.1
S5	11.6	4x7	40μm	1.5	0.1
S6	13.5	4x7	40μm	1.5	0.1
S7	11.6	4x7	40μm	1.5	0.1

Table 5: *A comparison between the experimental (Ω_a) and the simulated(Ω_{GATE}) solid angle values for the detectors used in the experimental analysis where, N_a is the number of counts of the alpha peak and t is the record time.*

Detector	t (sec)	N_α (Counts)	Ω_α (sr)	Ω_{GATE} (sr)	Variation
M1	1080	429	1.247E-04	1.774E-04	29.7%
M2	1080	395	1.148E-04	1.774E-04	35.2%
T1-E	1680	11260	2.105E-03	2.584E-03	18.5%
T2-E	1260	8888	2.215E-03	2.582E-03	14.2%
T3-E	840	4673	1.747E-03	2.621E-03	33.3%

Table 6: *A comparison between the Ω_m/Ω ratio calculated by the known activity of Americium source [$(\Omega_m/\Omega)_a$] and via GATE simulation [$(\Omega_m/\Omega)_{GATE}$] for the detectors used in the data analysis.*

Detector	$(\Omega_m/\Omega)_\alpha$	$(\Omega_m/\Omega)_{GATE}$	Variation (%)
T1-E	5.927E-02	6.864E-02	-13.70
T2-E	5.185E-02	6.868E-02	-24.50
T3-E	6.574E-02	6.767E-02	-2.80

Using Eq. (3.3) and the data of Table 6, the cross sections for the transfer reaction channels were calculated as appear in Tables 7-12. The uncertainties in cross sections were calculated according to the following formula:

$$\Sigma = \pm\sqrt{\left(\frac{\partial\sigma(\theta)}{\partial N}\sigma_N\right)^2 + \left(\frac{\partial\sigma(\theta)}{\partial N_m}\sigma_{Nm}\right)^2 + \left(\frac{\partial\sigma(\theta)}{\partial\Omega}\sigma_\Omega\right)^2 + \left(\frac{\partial\sigma(\theta)}{\partial\Omega_m}\sigma_{\Omega m}\right)^2} \Rightarrow$$

$$\Sigma = \pm\sigma(\theta)\sqrt{\frac{1}{N} + \frac{1}{N_m} + \frac{N_a\Sigma_t^2 + t^2}{t^2 N_a} + \frac{N_{am}\Sigma_t^2 + t_m^2}{t_m^2 N_{am}}}$$

(3.5)

where:

$\sigma(\theta)$ is the cross section,

N is the number of counts of the transfer peak,

N_a is the number of counts of the alpha peak for each detector,

t is the record time and

σ_t is the error in time measurement ($\approx$30sec.)

The index m is referred to the monitor information.

The last two terms of Eq.(3.5) are relevant to the error in the solid angle which was calculated via Eq. (3.4). Thus, time dependence is introduced to the overall uncertainty ($\mathbf{t}$ and $\mathbf{t_m}$). The contribution of these terms to the overall uncertainty is about 5%. It should be noted, that using the two monitors (M1,M2) at symmetrical positions, we succeeded to minimize the error due to diversity of the beam, and both due to the target thickness and the flux of the beam (DΦ). As the statistics at the angular position $\pm 20^o$ was high, the factor ($1/N_m$) has a small contribution to the overall uncertainty. The error propagation formula is presented in detail on the Appendix III.

In principle, the cross sections were determined via telescope information, placed at symmetrical positions. The final values, shown in Tables 7-12 represent in most of the cases a *weighted mean cross section* [57] formed as:

$$\sigma(\theta)_{mean} = \frac{\sum_i\left(\dfrac{\sigma(\theta)_i}{\Sigma_i^2}\right)}{\sum_i\left(\dfrac{1}{\Sigma_i^2}\right)}$$

(3.6)

and

$$\Sigma_{mean} = \cfrac{1}{\sum\limits_{i}\left(\cfrac{1}{\Sigma_i^2}\right)}$$

(3.7)

where:

$\sigma(\theta)$ is the cross section and

Σ is the error in the cross section value.

The measured cross sections are referred to the laboratory system. Therefore, a system transformation was necessary to evaluate the cross sections at the center of mass system. That was performed via a routine in *C*, details of which are given on the Appendix IV.

Table 7*: Cross sections calculations for the reaction ^{28}Si ($^{20}Ne,^{24}Mg)^{24}Mg$ at 52.3 MeV.*

Θ_{lab}(deg)	Θ_{cm}(deg)	σ_{lab}(mb)	σ_{cm}(mb)	Error	Error %
37.00	69.97	0.0599	0.0206	0.0073	35.61
40.00	73.36	0.0689	0.0102	0.0044	42.79
47.00	85.73	0.0050	0.0021	0.0016	77.32

Table 8*: Cross sections calculations for the reaction ^{28}Si ($^{20}Ne,^{24}Mg)^{24}Mg$ at 70.0 MeV*

Θ_{lab}(deg)	Θ_{cm}(deg)	σ_{lab}(mb)	σ_{cm}(mb)	Error	Error %
30.00	55.26	0.0968	0.0324	0.0116	35.87
35.00	64.30	0.0726	0.0257	0.0062	23.94
40.00	73.26	0.0953	0.0359	0.0141	39.29
45.00	82.10	0.0303	0.0117	0.0025	21.01
50.00	90.80	0.0470	0.0212	0.0044	20.90
55.00	99.32	0.0141	0.0064	0.0014	22.72

Table 9*: Cross sections calculations for the reaction ^{28}Si ($^{20}Ne,^{16}O)^{32}S$ at 52.3 MeV.*

Θ_{lab}(deg)	Θ_{cm}(deg)	σ_{lab}(mb)	σ_{cm}(mb)	Error	Error %
25.00	39.15	0.6915	0.3004	0.0430	14.31
27.00	42.22	0.3702	0.1631	0.0164	10.06
33.00	51.36	0.0979	0.0452	0.0067	14.82
47.00	72.00	0.6700	0.3591	0.0793	22.08
50.00	76.29	0.3886	0.1812	0.0267	14.71
60.00	90.04	0.2824	0.1834	0.0700	38.17

Table 10: *Cross sections calculations for the reaction ^{28}Si ($^{20}Ne,^{16}O)^{32}S$ at 70.0MeV.*

Θlab(deg)	Θcm(deg)	σ_{lab}(mb)	σ_{cm}(mb)	Error	Error %
25.00	39.30	0.7472	0.3224	0.0480	14.89
30.00	46.99	0.4193	0.1875	0.0320	17.07
35.00	54.58	0.3699	0.1727	0.0260	15.06
40.00	62.06	0.3542	0.1682	0.0380	22.59
45.00	69.40	0.4717	0.2133	0.0620	29.07
50.00	76.29	0.1087	0.0606	0.0160	26.40

Table 11: *Cross sections calculations for the reaction ^{28}Si ($^{20}Ne,^{12}C)^{36}Ar$ at 52.3MeV.*

Θ_{lab}(deg)	Θ_{cm}(deg)	σ_{lab}(mb)	σ_{cm}(mb)	Error	Error %
27.00	39.49	0.2848	0.1417	0.0193	13.59
30.00	43.78	0.2202	0.1117	0.0290	25.98
33.00	48.04	0.1333	0.0691	0.0107	15.49
35.00	50.86	0.1873	0.0985	0.0263	26.70
37.00	53.66	0.1635	0.0874	0.0441	50.47
40.00	57.83	0.1520	0.0790	0.0166	21.00
47.00	67.39	0.1936	0.1139	0.0116	10.17
50.00	71.40	0.1221	0.0743	0.0118	15.86
55.00	77.96	0.1615	0.0861	0.0103	12.02
65.00	90.56	0.0526	0.0390	0.0121	30.94

Table 12: *Cross sections calculations for the reaction ^{28}Si ($^{20}Ne,^{12}C)^{36}Ar$ at 70.0MeV.*

Θ_{lab}(deg)	Θ_{cm}(deg)	σ_{lab}(mb)	σ_{cm}(mb)	Error	Error %
25.00	36.72	0.1557	0.0762	0.0279	36.67
35.00	50.99	0.0968	0.0507	0.0132	26.11
40.00	57.98	0.1933	0.1057	0.0412	38.96
45.00	64.85	0.0617	0.0354	0.0144	40.68
50.00	71.58	0.1643	0.0892	0.0226	25.36

The analysis of the data was performed in the *DWBA* framework with the code *FRESCO*. In the next chapter, some simple *DWBA* calculations for the transfer reactions mentioned above are included where, several trials using different kinds of potentials were performed in order to deduce the optical potential for the system $^{20}Ne+^{28}Si$.

4. Theoretical analysis

As it was mentioned on chapter 1, transfer reaction calculations are strongly dependent on the entrance potential, playing a major complementary role to elastic scattering for deducing the optical potential (see e.g [64]). Into this context, a potential proposed from the elastic scattering of ^{20}Ne+^{28}Si at near barrier energies, was validated via the transfer reaction results. For that, simple *DWBA* calculations were performed via the code *FRESCO* for the one alpha pick-up and stripping reactions as well for the one ^{8}Be transfer reaction.

In more detail, in a parallel analysis in this laboratory [65], three sets of potentials were adopted in order to determine the ^{20}Ne+^{28}Si optical potential. In a macroscopic approach, *Woods-Saxon* form factors were adopted for the real part,-one with a deep and one with a shallow depth- while in a microscopic approach the *BDM3Y1* interaction was considered. For the easiness of the procedure in the present study this interaction was fitted by a *Woods-Saxon* form factor. Also, *Woods-Saxon* form factors were adopted for the imaginary part of all three optical potentials. The results of the optical model analysis are presented in Tables (13 and 14) as *set I*, *set II* and *set III* corresponding to the deep potential, the shallow one and the *BDM3Y1* interaction respectively. In all cases, the depth of the imaginary potential is shallow, indicating that, direct reactions are dominant compared to the compound nucleus ones.

Table 13: *Optical model parameters extracted from fits to the elastic scattering data of ^{20}Ne+^{28}Si at the energy of 52.3 MeV, where V, W, R and a are the depths, the radius and the diffusivity respectively (Table from V. Soukeras: Private communication).*

Potential	V_0(MeV)	R_V(fm)	a_V(fm)	W_0(MeV)	R_W(fm)	a_W(fm)
Set I	150.00	6.516	0.575	2.50	8.419	0.248
Set II	20.41	7.292	0.570	2.44	6.844	0.160
Set III	52.77	5.883	0.816	1.458	8.069	0.198

Table 14: *Optical model parameters extracted from fits to the elastic scattering data of ^{20}Ne+^{28}Si at the energy of 70 MeV, where V, W, R and a are the depths, the radius and the diffusivity respectively (Table from V. Soukeras: Private communication).*

Potential	V_0(MeV)	R_V(fm)	a_V(fm)	W_0(MeV)	R_W(fm)	a_W(fm)
Set I	150.00	6.516	0.575	3.90	8.800	0.248
Set II	20.41	7.120	0.570	4.84	6.844	0.160
Set III	32.60	5.763	0.828	1.102	8.011	0.309

Subsequently, the obtained optical potentials were fed as entrance potential in the transfer reaction calculations in order to validate them and the results will follow. Before that, some general characteristics about our *DWBA* calculations are presented bellow.

The basic ingredients required to calculate the transfer amplitude in the *DWBA* approximation is the interacting potentials and the wave functions for the initial and final states. As the effective potential, responsible for the transfer process, acts only on the transferred particle wave function, a cluster model was adopted in both entrance and exit channel where, the projectile is assumed to be a valence particle bound to a core nucleus. Into this context, the appropriate binding potentials were taken from the literature and are presented in Table 16. In this model, the wave function of the composite nucleus occurs to be a superposition of the valence and the core nucleus wave functions [41] (Eq. 4.1).

$$\Phi_{comp}(\xi,\vec{r}) = \frac{1}{\sqrt{n_C}} \sum_{\ell,I,j} A_{\ell sj}^{IJ} \left[\Phi_{core}(\xi) \otimes \varphi_{\ell sj}(\vec{r}) \right] \quad (4.1)$$

where

Φ_{comp}: is the wave function of the composite nucleus,

Φ_{core}: is the wave function of the core nucleus,

$\varphi_{\ell sj}$: is the wave function of the transferred particle,

$A_{\ell sj}$: is the spectroscopic amplitude

n_c: is the number of cluster in the composite nucleus and

ξ: represents the internal variables of the core.

As a result, the wave function of the transferred particle has to be constructed and thus, the quantum numbers (ℓ,s,j) of the assumed valence state in the core nucleus and the number of nodes (nn) of the wave function should be specified in the code. The number of nodes of the wave function was evaluated through *Talmi-Moshinki* transformation [66,67], obeying at Eq. (4.2).

$$2(N-1) + L = \sum_{i=1}^{k} \left[2(n_i - 1) + \ell_i \right] \quad (4.2)$$

In the above formula *N* is the number of nodes, *L* is the angular momentum of the valence particle in the composite nucleus, *k* is the number of transferred nucleons while, *n* and ℓ is the principle and the angular momentum quantum number respectively.

As it is seen above (Eq. 4.1), a quantity of great importance for our calculation is *the spectroscopic amplitude* for the overlap <composite nucleus | core nucleus>. Its square module, called *spectroscopic factor*, can be considered as the probability of finding the alpha particle in a well defined state (ℓ,s,j) coupled to the core [41].

Therefore, for each overlap included in our calculations, the alpha and ^{8}Be spectroscopic factors are listed in Table 15.

Table 15: Alpha and ^{8}Be spectroscopic factors for the transfer overlaps.

Overlap	Spectroscopic factor	Work
$<^{20}$Ne$|^{16}$O$>$	0.71	Ref. [68]
$<^{32}$S$|^{28}$Si$>$	0.33	Ref. [69]
$<^{24}$Mg$|^{20}$Ne$>$	0.21	Ref. [70]
$<^{28}$Si$|^{24}$Mg$>$	0.52	Ref. [70]
$<^{20}$Ne$|^{12}$C$>$	0.64	This work
$<^{36}$Ar$|^{28}$Si$>$	0.25	This work

Table 16: The binding potentials included in the DWBA calculations.

Core-Valence	V$_0$(MeV)	R$_V$(fm)	a_V(fm)	W$_0$(MeV)	R$_W$(fm)	a_W(fm)	Reference
^{16}O-alpha	179.10	5.380	0.590	31.10	4.928	0.820	[71]
^{24}Mg-alpha	113.30	5.568	0.792	18.18	7.021	0.634	[72]
^{12}C-^{8}Be [a]	60.10	5.065	0.600	32.60	5.065	0.600	[73]

[a] The ^{12}C-^{8}Be binding potential was approximated with the ^{12}C-^{9}Be one.

4.1. One alpha transfer calculations

4.1.1. ^{28}Si (^{20}Ne, ^{16}O)^{32}S

For the one-alpha stripping reaction we have assumed the simplest cluster structure for the projectile. The ^{20}Ne was modeled as a ^{16}O core and a valence alpha particle. Therefore, besides the ^{20}Ne+^{28}Si interaction, our calculation included the binding potential between the ^{16}O and the alpha [71], the potential between the alpha and the ^{28}Si [74], the potential between the ^{16}O and the ^{28}Si [75] and finally the potential describing the elastic scattering at the exit channel [76].

Based on the model described above, a simple *DWBA* calculation for the reaction **^{28}Si (^{20}Ne,^{16}O)^{32}S** was performed for the energy of 52.3 MeV and the results are shown in Figure 24*a* together with the elastic scattering data presented as Figure 24*b*. Results adopting *set I*, *set II* and *set III* (Table 13) as entrance potentials are denoted with the blue dotted, the red dashed, and the green solid curve respectively.
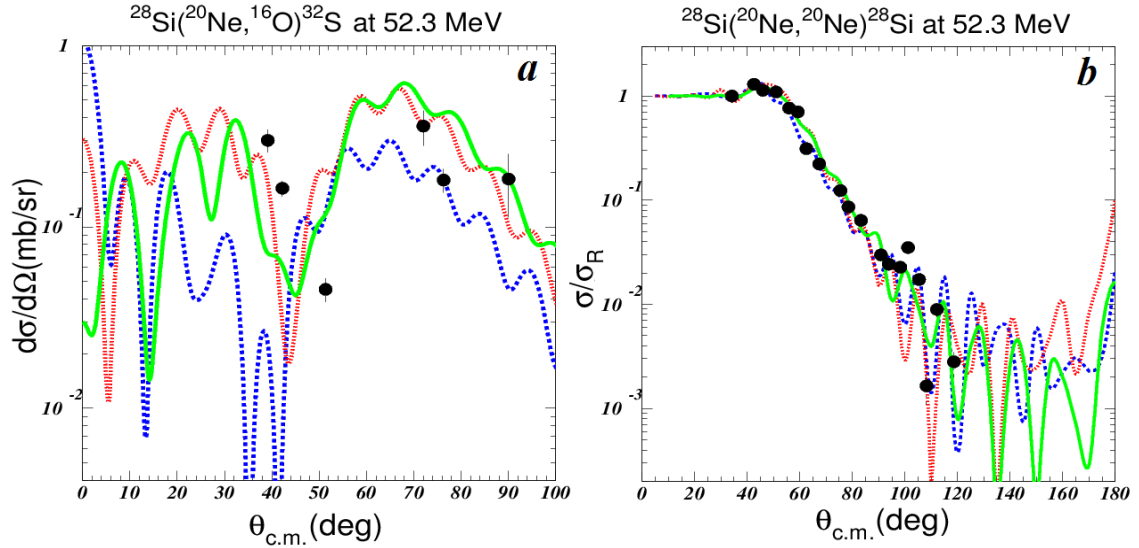
Figure 24: *a) Angular distribution data for the transfer reaction $^{28}Si(^{20}Ne,^{16}O)^{32}S$ measured at 52.3 MeV are compared with simple DWBA calculations. The blue, red and green curves represent calculations using as entrance potential set I, set II and set III respectively. b) Angular distribution data for the $^{28}Si(^{20}Ne,^{20}Ne)^{28}Si$ elastic scattering measured at 52.3 MeV are compared with optical model calculations. In all cases, the calculations were performed adopting the same kind of potential like Figure 24a (Figure from V. Soukeras: private communication).*
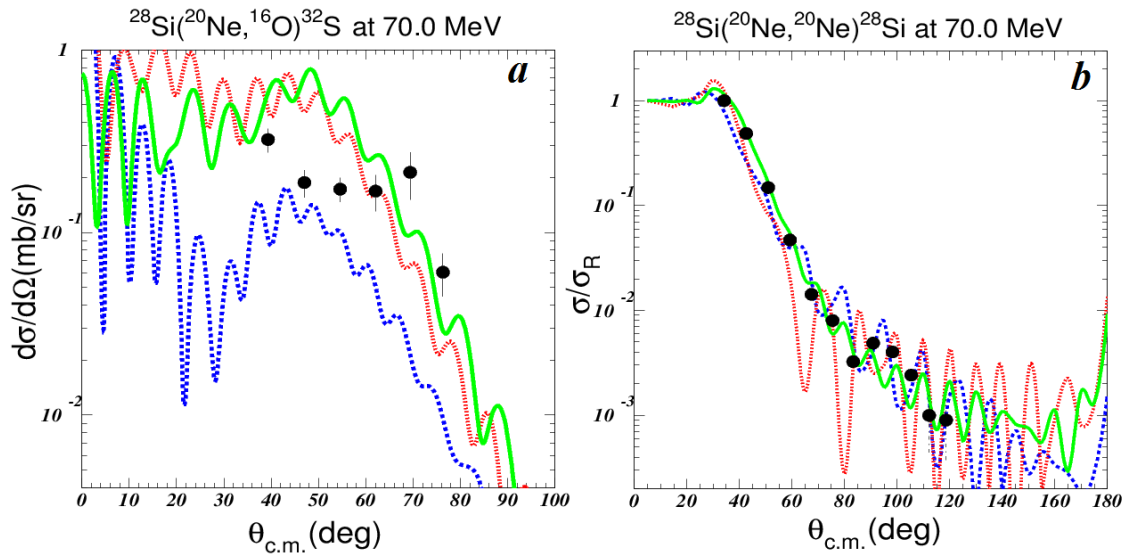
Figure 25: *a) Angular distribution data for the transfer reaction $^{28}Si(^{20}Ne,^{16}O)^{32}S$ measured at 70 MeV are compared with simple DWBA calculations. The blue, red and green curves represent calculations using as entrance potential set I, set II and set III respectively. b) Present angular distribution data for the $^{28}Si(^{20}Ne,^{20}Ne)^{28}Si$ elastic scattering measured at 70 MeV are compared with optical model calculations. In all cases, the calculations were performed adopting the same kind of potential like Figure 25a (Figure from V. Soukeras: Private communication).*

In principle, for both energies at 52.3 and 70 MeV, potentials denoted in Tables 13 and 14 by *set II* and *set III* that is the shallow macroscopic and the microscopic one, are the most adequate to describe both elastic scattering and transfer reaction data. However the limited angular range in the angular distribution and the poor angular resolution prevented us for drawing firm conclusion for the optical potential.

4.1.2. ^{28}Si (^{20}Ne, ^{24}Mg)^{24}Mg

In the case of the specific pick-up reaction, the silicon nucleus was modeled as a ^{24}Mg core and a valence alpha particle. Into this context, it was necessary to introduce in the *DWBA* calculation the binding potential of the valence alpha particle in the ^{24}Mg nucleus [72], the alpha-projectile interaction [72] and the core-product potential [77]. It should be noted that it was not available an optical potential describing the core-core interaction (^{20}Ne-^{24}Mg). Thus, to a first approximation the ^{20}Ne+^{28}Si potential was used. Simple *DWBA* calculations for the reaction ^{28}Si (^{20}Ne, ^{24}Mg) ^{24}Mg at the energy of 52.3 and 70 MeV are presented in Figure 26*a* and 27*a* respectively.
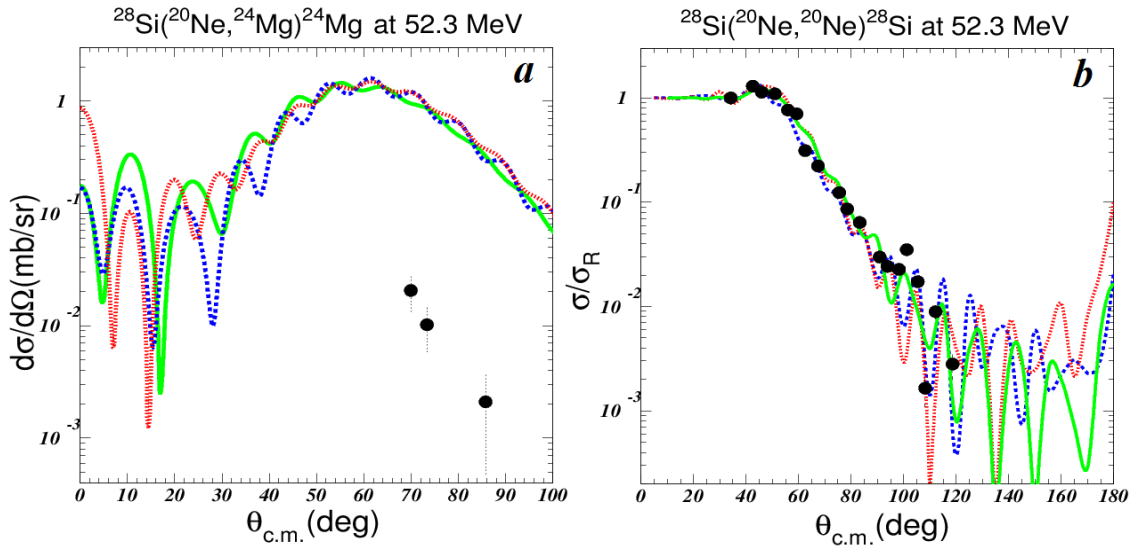
Figure 26: *a) Angular distribution data for the transfer reaction ^{28}Si (^{20}Ne,^{24}Mg)^{24}Mg measured at 52.3 MeV are compared with simple DWBA calculations. The blue, red and green curves represent calculations using as entrance potential set I, set II and set III respectively .b) Angular distribution data for the ^{28}Si(^{20}Ne,^{20}Ne)^{28}Si elastic scattering measured at 52.3 MeV are compared with optical model calculations. In all cases, the calculations were performed adopting the same kind of potential like Figure 26a (Figure from V. Soukeras: Private communication).*
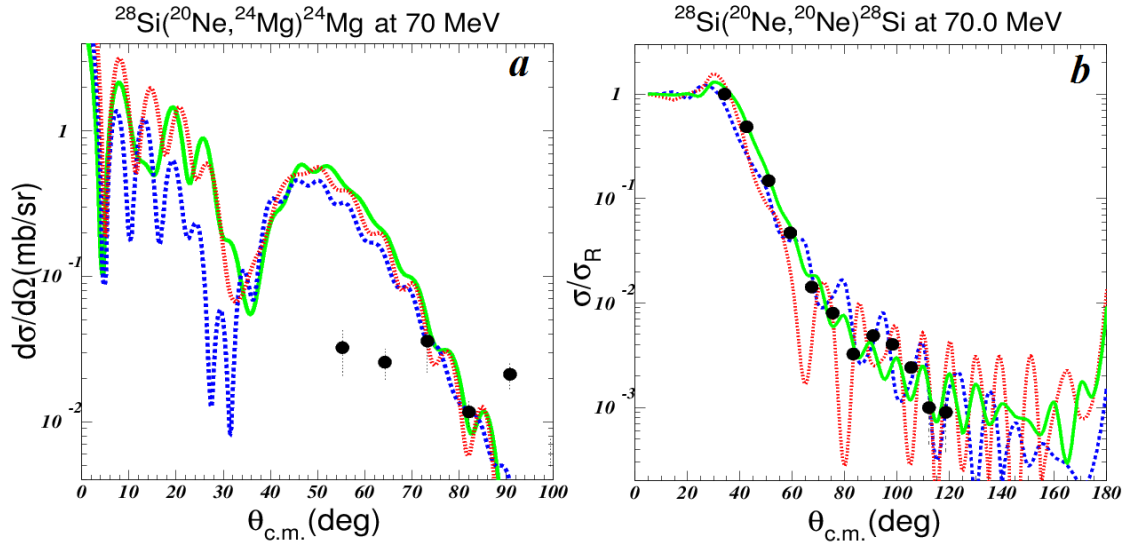
Figure 27: *a) Angular distribution data for the transfer reaction ^{28}Si $(^{20}$Ne,^{24}Mg$)$ ^{24}Mg measured at 70 MeV are compared with simple DWBA calculations. The blue, red and green curves represent calculations using as entrance potential set I, set II and set III respectively. b) Present angular distribution data for the ^{28}Si $(^{20}$Ne, ^{20}Ne$)^{28}$Si elastic scattering measured at 70 MeV are compared with optical model calculations. In all cases, the calculations were performed adopting the same kind of potential like Figure 27a (Figure from V. Soukeras: Private communication).*

In principle, the results of this *DWBA* calculation do not describe adequately well the data. Specifically at the energy of 52.3 MeV, the number of experimental points is insufficient and present large errors preventing us for validating the potential. At the energy of 70 MeV the situation is a little better, as the predicted cross sections have the same magnitude as the experimental ones, giving some support to the proposed potential by elastic scattering.

4.2. ^{8}Be transfer calculations

As it was mentioned on chapter 3, in the carbon contour we identified ^{12}C nuclei due to the week reaction channel **^{28}Si (^{20}Ne, ^{12}C)^{36}Ar**. The analysis of this was performed in the *DWBA* framework. Based on preliminary *DWBA* calculations, performed by Dr. Nick Keeley [78], it was found that the sequential transfer of two alphas from ^{20}Ne to the ^{28}Si nucleus could not describe properly the intensity of the specific reaction channel. Thus, we assumed that a whole ^{8}Be is transferred from the projectile to the target before breakup to two alphas.

In our calculation ^{20}Ne nucleus was modeled as a valence ^{8}Be bound to the ^{12}C core nucleus. Also, it was necessary to introduce the core-core potential (^{12}C- ^{28}Si) [79], the valence-target interaction [80] and the core-product potential [81]. It should be noted that due to the unbound nature of ^{8}Be, the binding potential between ^{12}C and ^{8}Be nucleus is unknown. Thus, to a first approximation as a binding

potential we used the ^{12}C-^{9}Be potential [73]. Furthermore, appropriate spectroscopic factors for the <^{20}Ne|^{12}C> and <^{36}Ar|^{28}Si> overlaps were not available and were fitted to the data. The obtained values are shown in Table 15. The results of the *DWBA* calculations are presented in Figure 28*a* and 29*a* for the energy of 52.3 and 70 MeV respectively.

At the energy of 52.3 MeV, clearly *set III* provides a better fit to the data. This fact is in agreement with the results of the elastic scattering analysis where, the specific potential describes the data behavior better than the other two do. The one beryllium transfer data are well reproduced so, one can say that *set III* is capable of describing the elastic scattering at the entrance channel. On the other hand, at the energy of 70 MeV, the lack in experimental data prevent us from draw any firm conclusions. However, *set III* is able to describe cross sections magnitudes indicating its validity. The fact that the predicted cross sections do not vary unreasonably from the experimental ones, indicates that the proposed optical potential is capable of describing elastic scattering at the entrance channel. However, to confirm this scenario, more experimental points are necessary.
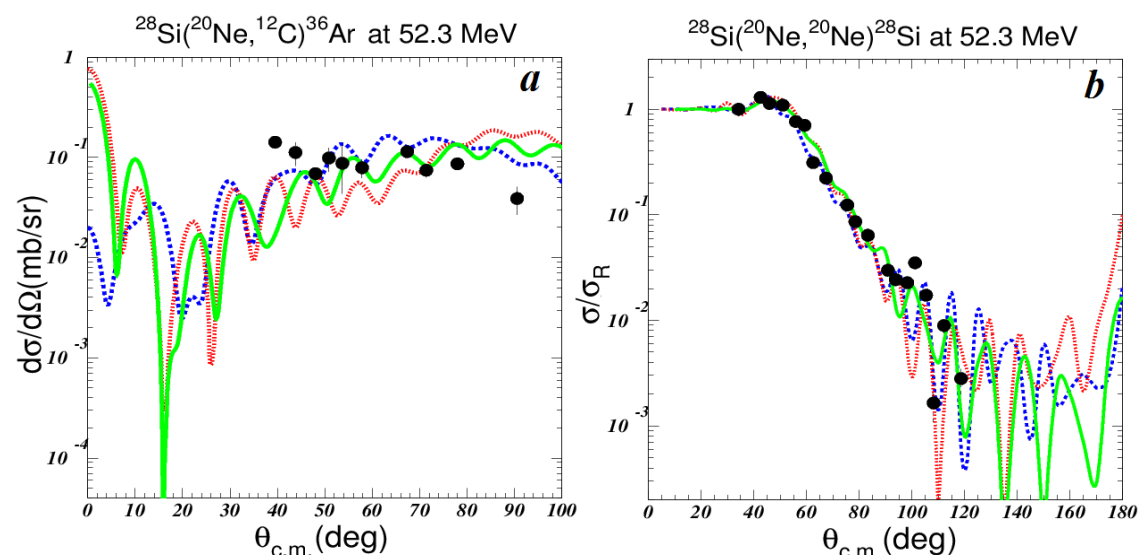
Figure 28: *a) Angular distribution data for the transfer reaction ^{28}Si(^{20}Ne,^{12}C)^{36}Ar measured at 52.3 MeV are compared with simple DWBA calculations. The blue, red and green curves represent calculations using as entrance potential set I, set II and set III respectively. b) Angular distribution data for the ^{28}Si(^{20}Ne,^{20}Ne)^{28}Si elastic scattering measured at 52.3 MeV are compared with optical model calculations. In all cases, the calculations were performed adopting the same kind of potential like Figure 28a (Figure from V. Soukeras: Private communication).*
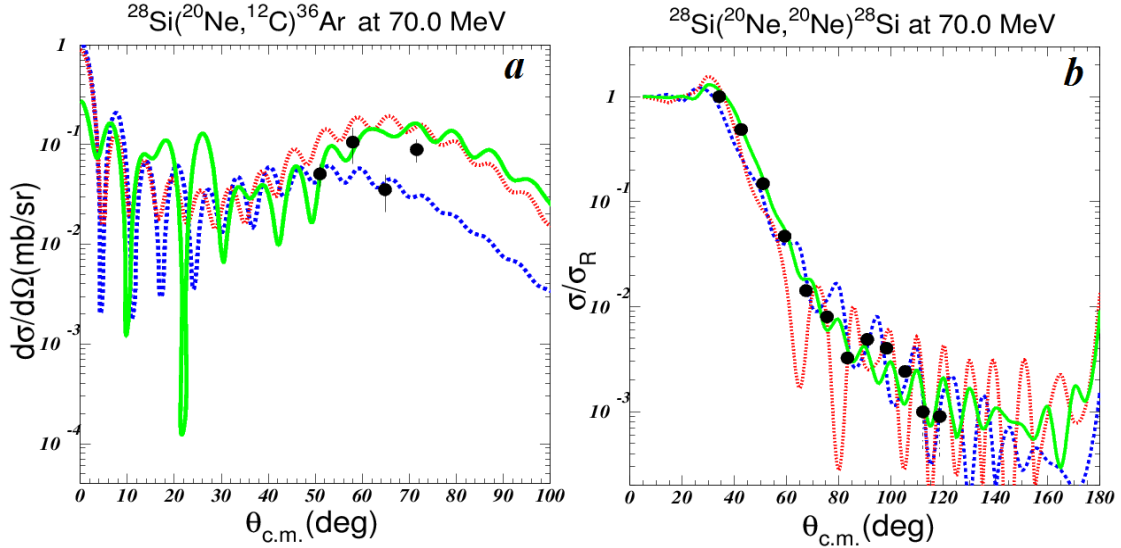
Figure 29: *a) Angular distribution data for the transfer reaction ^{28}Si $(^{20}Ne,^{12}C)$ ^{36}Ar measured at 70 MeV are compared with simple DWBA calculations. The blue, red and green curves represent calculations using as entrance potential set I, set II and set III respectively. b) Present angular distribution data for the ^{28}Si $(^{20}Ne, ^{20}Ne)$ ^{28}Si elastic scattering measured at 70 MeV are compared with optical model calculations. In all cases, the calculations were performed adopting the same kind of potential like Figure 29a (Figure from V. Soukeras: Private communication).*

4.3. Coupled reaction channels calculations

In a simultaneous *Coupled Reaction Channels* framework (*CRC*), Nick Keeley described both elastic scattering as well as transfer data at the energy of 52.3 MeV. In order to provide a reasonable description of the elastic scattering data, transfer couplings to the elastic channel have been also considered. In the case of the pick-up reaction, besides the ground state, inelastic excitations in the 2^+ state of the ^{24}Mg residue nuclei in the $^{24}Mg+^{24}Mg$ partition and of the ^{32}S nucleus in the $^{16}O +^{32}S$ partition were also considered. Finally, the elastic transfer of a ^{8}Be cluster was taken into account in order to provide a better description of the elastic scattering data. The results of the *CRC* calculations for the transfer reactions are illustrated in Figure 30.

In principle, the *CRC* calculations provided a better description of the transfer data than the simple *DWBA* ones. This is quite expected since the *CRC* calculation takes into account transition matrix elements between the coupled channels [82], while in the *DWBA* one, the transition matrix depends upon the entrance and the exit channel. So, it is expected that the *CRC* calculation will be more accurate. This fact is more obvious in case of the alpha pick-up reaction. Although the number of experimental data is limited, we may state that the *CRC* calculations describe the angular distribution with more success.

Only in case of the inverse process, the alpha stripping reaction, the simple *DWBA* seems to reproduce better the angular distribution, but where couplings to reaction channels are simply simulated by the imaginary potential. In the *CRC*

approach all the identified reaction channels are included in detail and a small uncertainty in a spectroscopic factor or in a binding potential may cause a big problem in the calculation itself.
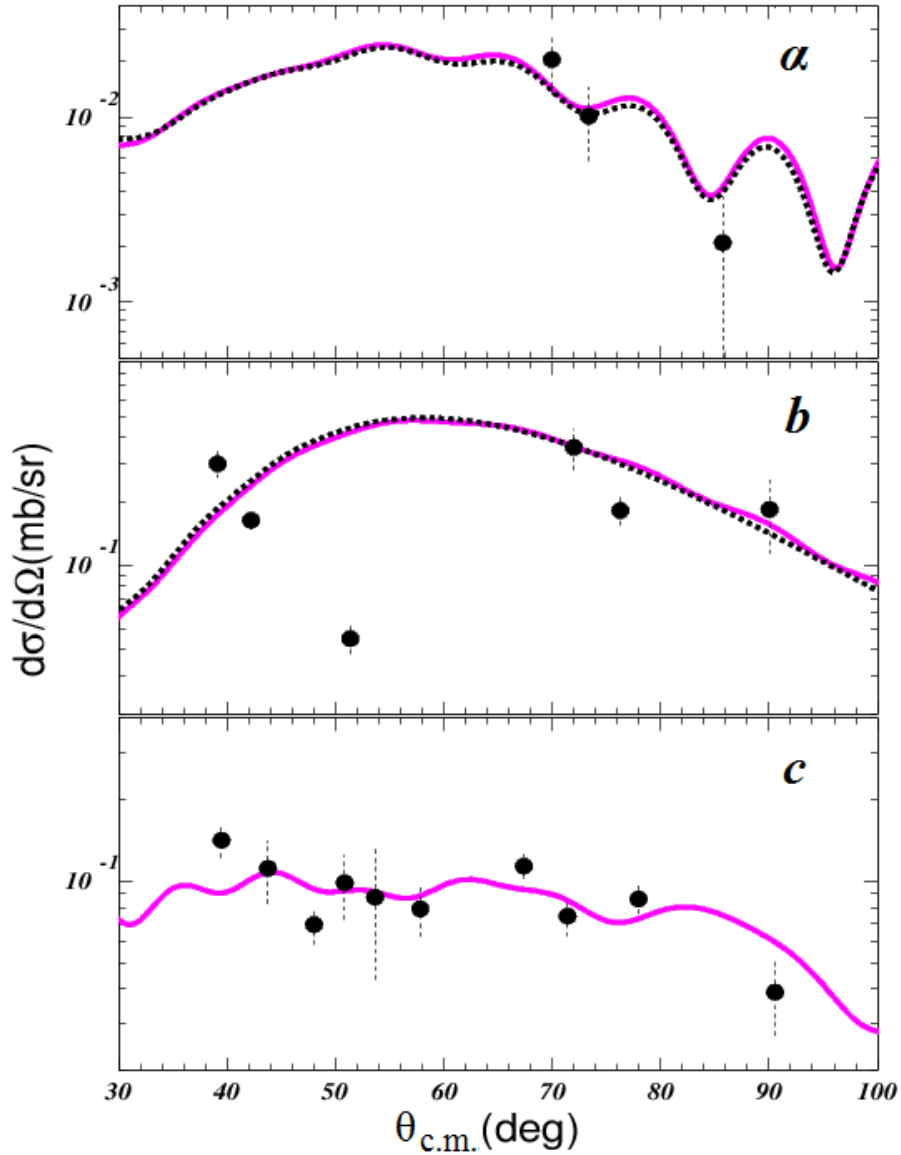
Figure 30: *Present angular distribution data for the $^{28}Si(^{20}Ne,^{24}Mg)^{24}Mg$ (a), $^{28}Si(^{20}Ne,^{16}O)^{32}S$ (b) and $^{28}Si(^{20}Ne,^{12}C)^{36}Ar$ (c) measured at the energy of 52.3 MeV. The solid lines represent the full calculations while the dashed ones calculations that do not include a direct ^{8}Be cluster elastic transfer (Figure from N. Keeley: Private communication).*

5. Summary and conclusions

Transfer angular distribution measurements for the system ^{20}Ne+^{28}Si were performed at 52.3 and 70 MeV at the Heavy Ion Laboratory of University of Warsaw. Angular distributions corresponding to one alpha pick-up and stripping reactions as well as to an ^{8}Be stripping reaction were obtained. The data were analyzed in the *DWBA* framework, by using as entrance potentials the suggested ones from a parallel analysis on the elastic scattering data.

It was found that the one alpha transfer data are described adequately well by two of the adopted entrance potentials, the shallow macroscopic potential and the microscopic one, described by a *BDM3Y1* interaction. In principle, for the ^{8}Be transfer reaction the data are mainly reproduced by the microscopic description. Specifically, at the energy of 52.3 MeV, the *DWBA* calculation clearly provides a better fit to the data by using the microscopic interaction, while at the energy of 70 MeV, the limited number of data prevent us from drawing any concrete conclusion.

In summary, we have validated the optical potential for the system ^{20}Ne+^{28}Si, deduced by elastic scattering data, performing simple *DWBA* calculations. The best potential was found to be a microscopic one, described by a *BDM3Y1* interaction.

Finally, a parallel analysis of the data was performed in the *CRC* framework by Dr. Nick Keeley providing in general a better description of the transfer angular distributions. Strong point of these calculations, leading to a simultaneous description of both elastic scattering and transfer reactions, proved to be the inclusion of elastic transfer of a ^{8}Be nucleus from the target to the projectile, to coupling mechanisms. So, the *CRC* analysis of the elastic scattering data suggests significant ^{8}Be clustering in the ground state of ^{28}Si nucleus, while the same analysis of the ^{28}Si (^{20}Ne,^{12}C)^{36}Ar data suggests significant ^{8}Be clustering of ^{20}Ne and ^{36}Ar nuclei.

References – Bibliography

[1] *S. T. Butler, **Phys. Rev. 85**, 1095 (1950).*

[2] *T. Yamaya, S. Ohkubo, S. Okabe, M. Fujiwara, **Phys. Rev. C47**, 2389 (1993).*

[3] *F. D. Becchetti, et al., **Kyoto Conference**, Contributed Papers, p. 410 (1988).*

[4] *L. Buchmann, **The Astrophysical Journal**, **468**: L127–L130 (1996).*

[5] *A. M. Kobos et al., **Nucl. Phys. A395**, 248 (1983).*

[6] *P. Braun - Munzinger and J. Barrette, **Phys. Reports 87**, 209 (1982).*

[7] *U. C. Voos et al., **Nucl. Phys. A135**, 207 (1969).*

[8] *M. El-Azab Farid et al**, Nucl. Phys. A691**, 671 (2001).*

[9] *G .R. Satchler and W. G. Love, **Phys. Reports 55**, 183 (1979).*

[10] *A. Lépine – Szily et al., **Phys. Lett. B304**, 45 (1993).*

[11] *V. N. Bragin and R. Donangelo, **Nucl. Phys. A454**, 409 (1986).*

[12] *P. Braun-Munzinger and J. Barrette, **in Proceedings of the Symposium on Heavy-Ion Elastic Scattering**, Rochester 2977, edited by R. M. DeVries (University of Rochester, Rochester, 1977), p. 85.*

[13] *P. Braun-Munzinger et al., **Phys. Rev. C24**, 1010 (1981).*

[14] *W. Von Oertzen et al., **Phys. Lett. B26**, 291 (1968).*

[15] *A. Gobbi et al., **Nucl. Phys. A112**, 537 (1968).*

[16] *A. Lépine-Szily et al., **Phys.Rev. Lett. 82**, 3972 (1999).*

[17] *R. Bock and H. Yoshida, **Nucl. Phys. A189**, 177 (1972).*

[18] *G. R. Satchler, Direct Nuclear Reactions, Oxford University Press, Oxford, 1983.*

[19] *K. -I. Kubo and M. Hirata, **Nucl. Phys. A187**, 186 (1972).*

[20] *M. Paul et al., **Phys. Rev. Lett. 40**, 1310 (1978).*

[21] *F. Schmittroth and W. Tobocman, **Phys. Rev. C1**, 377 (1970).*

[22] *R. N. Glover and A. D. W. Jones, **Phys. Lett. 18**, 165 (1965).*

[23] *A. Pakou et al., **Phys. Lett. B556**, 21 (2003).*

[24] *A. Pakou et al., **Phys. Rev. Lett. 90**, 202701 (2003).*

[25] *A. Pakou et al., **Phys. Rev. C69**, 054602 (2004).*

[26] *A. Pakou et al., **Phys. Rev. C69**, 057602 (2004).*

[27] *A. Pakou et al., **Phys. Rev. C71**, 064602 (2005).*

[28] *A. Pakou et al., **Journal of Phys. G 31**, S1723 (2006).*

[29] *A. Pakou et al., **Phys. Lett. B633**, 691 (2006).*

[30] *D. Roubos et al., **Phys. Rev. C73**, 051603 (2006).*

[31] *A. Pakou et al., **Nucl. Phys. A784**, 13 (2007).*

[32] *A. Pakou et al., **Phys. Rev. C76**, 054601 (2007).*

[33] *A. Pakou et al., **Phys. Rev. C78**, 067601 (2008).*

[34] *A. Pakou et al., **Eur. Phys. Journal A39**, 187 (2009).*

[35] *K. Zerva et al., **Phys. Rev. C80**, 017601 (2009).*

[36] *K. Zerva et al., **Phys. Rev. C82**, 044607 (2010).*

[37]   K. Zerva et al., **Eur. Phys. Journal A48**, 102 (2012).

[38]   R. R. Roy and B.P. Nigam, Nuclear Physics Theory and Experiment, John Wiley and Sons, Inc. (1967).

[39]   G. R. Satcher, Introduction to Nuclear Reactions, second edition (1990).

[40]   Leonard S. Rodberg and Roy M. Thaler, Introduction to the Quantum Theory of Scattering, Academic Press New York and London (1967).

[41]   I. J. Thomson, **Comp. Phys. Rep. 7**, 167 (1988).

[42]   R. D. Woods and D. S. Saxon, **Phys. Rev. 95**, 577 (1954).

[43]   C. M. Perey and F. G. Perey, **Phys. Rev. 152**, 923(1966).

[44]   P. R. Christensen and A. Winther, **Phys. Lett. 65B**, 19 (1976).

[45]   P. Braun-Munzinger et al., **Phys. Rev. Lett. 38**, 944 (1977).

[46]   P. Braun-Munzinger and J. Barrette, **Phys. Rep. 87**, 209 (1982).

[47]   W. Sciani et al., **Nucl. Phys. A620**, 91 (1997).

[48]   G. S. Malick, S. K. Agarwalla, B. Sahu and C. G. Shastry, **Phys. Rev. C73**, 054606 (2006).

[49]   A. M. Kobos and G. R. Satchler, **Nucl. Phys. A427**,589 (1984).

[50]   S. K. Agarwalla et al., **J. Phys. G: Nucl. Part. Phys. 32**, 165 (2006).

[51]   S. Y. Lee and Y-D Chan, **University of Washington preprint RLO–1388-743**, unpuplished (1977).

[52]   N. Alamanos and P. Roussel - Chomaz, **Ann Phys. Fr. 21**, 601 (1996).

[53]   Dao T. Khoa and W. von Oertzen, **Phys. Lett. B304**, 8 (1993).

[54]   W. D. Myers, **Nucl. Phys. A204**, 465 (1973).

[55]   Konrad Kleinknecht, Detectors for particle radiation, Cambridge University Press, second edition (1998).

[56]   Glenn F. Knoll, Radiation Detection and Measurements, John Wiley and Sons, Inc. third edition (2000).

[57]   William R. Leo, Techniques for Nuclear and Particle Physics Experiments: A How - to Approach, Springer-Verlag, second revised edition (1994).

[58]   A. Trzcinska and I. Strojek: private communication.

[59]   Application software group, Computer and Networks Division, CERN Program Library, PAW-Physics Analysis Workstation, CERN, Geneva, 1995.

[60]   V. I. Zagrebaev et al., OM code of NRV, **http://nrv.jinr.ru/nrv/**.

[61]   O. B. Tarasov, D. Bazin, **NIM B266**, 4657(2008).

[62]   S. Jan et al., **Phys. Med. Biol. 49**, 4543 (2004).

[63]   E. Stiliaris: private communication.

[64]   S. Kahana, B. T. Kim and M. Mermaz, **Phys. Rev. C20**, 2124 (1979).

[65]   V. Soukeras, Master Thesis candidate, private communication.

[66]   K. Rusek: private communication.

[67]   R. M. DeVries, **Phys. Rev. Lett. 30**,666 (1973).

[68]   T. Motobayashi et al., **Nucl. Phys. A331**, 193 (1979).

[69]   T. Madhusoodhanan et al., **J. Phys. G25**, 1897 (1999).

[70]   J. D. Cossairt et al., **Nucl. Phys. A261**, 373 (1976).

[71]   R. Jahn et al., **Phys. Lett. 65B**, (1976).

[72]   V. Avrigeanu, P. E. Hodgson and M. Avrigeanu, **Rhys. Rev. C49**, 4(1994).

[73]   *J. Carter et al.,* **Nucl. Phys. A591**, *349 (1995).*

[74]   *H. Wojciechowski,* **Phys. Rev. C72**, *044601 (2005).*

[75]   *I. Tserruya et al.,* **Nucl. Phys. A242**, *345 (1976).*

[76]   *J. C. Peng et al.,* **Nucl. Phys. A264**, *312 (1976).*

[77]   *H. Emling et al.,* **Nucl. Phys. A239**, *172 (1975).*

[78]   *N. Keeley: private communication.*

[79]   *C. M. Cheng et al.,* **Phys. Rev. C20**, *1042 (1979).*

[80]   *E. Mathiak et al,* **Nucl. Phys. A259**, *129 (1976).*

[81]   *A. Becker et al.,* **Nucl. Phys. A412**, *159 (1984).*

[82]   *T. Ohmnra et al.,* **Prog. Theor. Phys. 41**, *391(1969).*

Appendix

I. The code FRESCO

Since the *DWBA* calculations were performed with the code *FRESCO*, as an example the input file for the ^{28}Si(^{20}Ne,^{16}O)^{32}S reaction together with a description about the function of each line of the code are presented below.

Input file

Line 0	** 20Ne+28Si->16O+32S at Ebeam = 70.0 MeV
Line 1	0.04 25.0 0.10 0.100 9.3 -0.450
Line 2	00. 45. +.00 F F
Line 3	0 00.0 180. 0.5 -20.
Line 4	0.00 1 2 0 30 .000 0.0 0.0010
Line 5	1 1 0 0 1 3 0 0 0 1 0 0 1
Line 6	20Ne 19.992 10.0 1 28Si 27.97693 14.
Line 7	0.0 +1 0. 1.0 1 0.0 +1 0.00 F F
Line 8	16O 15.9949 8.0 1 32S 31.97207 16. 2.2170
Line 9	0.0 +1 0.0 0 2 0.0 +1 0.000 F F
Line 10	1 0 0 28. 20.0 1.300
Line 11	1 1 0 32.60 1.002 0.828 1.102 1.393 0.309
Line 12	2 0 0 32. 16.0 1.303
Line 13	2 1 0 100.0 1.22 0.500 30.00 1.250 0.400
Line 14	3 0 0 4. 16.00 1.300
Line 15	3 1 0 179.1 1.310 0.590 31.10 1.200 0.820
Line 16	4 0 0 4. 28.00 1.250
Line 17	4 1 0 75.62 1.130 0.47 8.390 1.130 0.470
Line 18	5 0 0 28. 16.00 1.35
Line 19	5 1 0 100.0 1.140 0.58 20.00 1.20 0.600
Line 20	0
Line 21	1 1 2 1 0 5 0 0.0 0.0 3 0 4.7340 1 1
Line 22	2 2 1 2 0 5 0 0.0 0.0 4 0 6.9480 1 1 0
Line 23	-2 1 7 0 -1 5
Line 24	1 1 1 1 0.8426
Line 25	-2 1 1 2 0.5745
Line 26	0 1 1
Line 27	70.0

- Line 0: Headline (it is not been read by the program).

- Line 1: Radial integration information.

- Line 2: Calculate coupled-channels sets in the interval 0≤J≤45

- Line 3: Printing settings for the cross sections.

- Line 4: Formalism choice.

- Line 5: Printing information for the output file.

- Line 6: Definition of the entrance channel.
- Line 7: Spin. parity and excitation energy for ^{20}Ne and ^{28}Si.
- Line 8: Definition of the exit channel.
- Line 9: Spin, parity and excitation energy for ^{16}O and ^{32}S.
- Line 10: Coulomb interaction at the entrance channel.
- Line 11: Optical potential for the entrance channel.
- Line 12: Coulomb interaction at the exit channel.
- Line 13: Optical potential for the exit channel.
- Line 14: Coulomb interaction for the core-valence nuclei.
- Line 15: Binding potential of the alpha particle in the ^{16}O core.
- Line 16: Coulomb interaction for the target-valence nuclei.
- Line 17: Optical potential for the target-valence nuclei.
- Line 18: Coulomb interaction for the core-core nuclei.
- Line 19: Optical potential for core-core nuclei.
- Line 20: Kept Blanc
- Line 21: The $<^{20}$Ne$|^{16}$O$>$ overlap information.
  - ➢ 1: Index of the information.
  - ➢ 1: Partition number of the composite nucleus.
  - ➢ 2: Partition number of the core nucleus.
  - ➢ 1: The overlap refers to the projectile (use "2" for target overlap).
  - ➢ 0: Take into account **J** couplings.
  - ➢ 5: Number of nodes of the wave function.
  - ➢ 0: Angular momentum of the alpha particle (**L**).
  - ➢ 0: Spin of the alpha particle (**S**).
  - ➢ 0: Total angular momentum of the alpha particle (**J**).
  - ➢ 3: Index of the binding potential ^{16}O-alpha (see Lines 14-15).
  - ➢ 0: Multiply the valence state wave function with the binding potential.
  - ➢ 4.7340: Binding energy of ^{20}Ne nucleus.
  - ➢ 1: Scale the volume term of binding potential to reproduce the binding energy.
  - ➢ 1: Printing settings.

- Line 22: The $<^{32}$S$|^{28}$Si$>$ overlap information.
- Line 23: Definition of the couplings.
  - ➢ -2: Partition number in which the alpha particle is transferred (The "-" symbol excludes couplings to the inverse direction).
  - ➢ 1: Partition number in which the alpha particle in originally located.
  - ➢ 7: Finite range transfer.

- ➢ 0: Use the post representation (use "1" for the prior representation).
  - ➢ -1: Use complex remnant potential.
  - ➢ 5: Index of the core-core potential (see Lines 18-19).
- Line 24: Definition of the $<^{20}Ne|^{16}O>$ overlap.
  - ➢ 1: The overlap refers to the projectile.
  - ➢ 1: The composite nucleus (^{20}Ne) is in its ground.
  - ➢ 1: The core nucleus (^{16}O) is in its ground state.
  - ➢ 1: Index of the "information line" about the overlap (see Line 21).
  - ➢ 0.8426: Spectroscopic amplitude for the $<^{20}Ne|^{16}O>$ overlap.
- Line 25: Definition of the $<^{32}S|^{28}Si>$ overlap.
  - ➢ -2: The overlap refers to the target (^{32}S) (The "-" symbol declares that no further overlaps will be constructed).
  - ➢ 1: The composite nucleus (^{32}S) is in its ground state.
  - ➢ 1: The core nucleus (^{28}Si) is in its ground state.
  - ➢ 2: Index of the "information line" about the overlap (see Line 22).
  - ➢ 0.5745: Spectroscopic amplitude for the $<^{32}S|^{28}Si>$ overlap.
- Line 26: Incoming channel energy.
  - ➢ 0: Default by the program.
  - ➢ 1: Number of partition including the incoming waves.
  - ➢ 1: The energy at the following line is referred to the projectile.
- Line 27: Energy of the reaction.

II. Gate simulation for the solid angle calculation

Geant4 is a toolkit for the simulation of the passage of particles through matter. Its areas of application include high energy, nuclear and accelerator physics, as well as studies in medical and space science. In the present work, the solid angle was also calculated by the program GATE, a simulation toolkit based on Geant4 Monte Carlo simulation. Here it is presented the input file we used in order to simulate the geometry of our detecting system.

<u>Input file</u>

```
#  Solid angle calculation via GATE simulation
#  for Si and gas detectors
#  UOI, December 2012

#
# V I S U A L I S A T I O N
#

/vis/open OGLSX
/vis/viewer/reset
/vis/viewer/set/viewpointThetaPhi   60  60
/vis/viewer/zoom  2.5
/vis/viewer/set/style surface
/vis/drawVolume
/tracking/storeTrajectory 1
/vis/scene/endOfEventAction accumulate
/vis/viewer/update
/gate/geometry/enableAutoUpdate


#
# W O R L D
#


/gate/world/geometry/setXLength  100 cm
/gate/world/geometry/setYLength  100 cm
/gate/world/geometry/setZLength  100 cm

#
# Detector Volumes
#


/gate/world/daughters/name SPECThead
/gate/world/daughters/insert box
/gate/SPECThead/geometry/setXLength          100.00 cm
/gate/SPECThead/geometry/setYLength          100.00 cm
/gate/SPECThead/geometry/setZLength          100.00 cm
/gate/SPECThead/placement/setTranslation   0.00  0.00  0.00 cm
/gate/SPECThead/setMaterial Vacuum
/gate/SPECThead/vis/setColor magenta
/gate/SPECThead/vis/forceWireframe
```

```
/gate/SPECThead/daughters/name mask
/gate/SPECThead/daughters/insert cylinder
/gate/mask/geometry/setRmin          0.00 cm
/gate/mask/geometry/setRmax          10.00 cm
/gate/mask/geometry/setHeight        0.50 cm
/gate/mask/placement/setTranslation  0.00  0.00 -10.50 cm
/gate/mask/setMaterial Aluminium
/gate/mask/vis/setColor grey
/gate/mask/vis/forceSolid

/gate/mask/daughters/name hole
/gate/mask/daughters/insert box
/gate/hole/geometry/setXLength        3.50 mm
/gate/hole/geometry/setYLength        10.50 mm
/gate/hole/geometry/setZLength        0.55 cm
/gate/hole/placement/setTranslation  0.00  0.00  0.00 cm
/gate/hole/setMaterial Vacuum
/gate/hole/vis/setColor magenta
/gate/hole/vis/forceWireframe


/gate/SPECThead/daughters/name tel
/gate/SPECThead/daughters/insert cylinder
/gate/tel/geometry/setRmin           00.00 cm
/gate/tel/geometry/setRmax            10.00 cm
/gate/tel/geometry/setHeight          20.00 cm
/gate/tel/placement/setTranslation   0.00  0.00  0.00 cm
/gate/tel/setMaterial Vacuum
/gate/tel/vis/setColor red
/gate/tel/vis/forceWireframe


/gate/tel/daughters/name myl1
/gate/tel/daughters/insert box
/gate/myl1/geometry/setXLength         5.00 cm
/gate/myl1/geometry/setYLength         5.00 cm
/gate/myl1/geometry/setZLength         2.50 um
/gate/myl1/placement/setTranslation  0.00  0.00  -9.90 cm
/gate/myl1/setMaterial Mylar
/gate/myl1/vis/setColor blue
/gate/myl1/vis/forceSolid


#/gate/tel/daughters/name gas
#/gate/tel/daughters/insert cylinder
#/gate/gas/geometry/setRmin            0.00 cm
#/gate/gas/geometry/setRmax            1.00 cm
#/gate/gas/geometry/setHeight          4.70 cm
#/gate/gas/placement/setTranslation  0.00  0.00  -7.50 cm
#/gate/gas/setMaterial Butane15mbar
#/gate/gas/vis/setColor yellow
#/gate/gas/vis/forceSolid


/gate/tel/daughters/name Det1
/gate/tel/daughters/insert cylinder
/gate/Det1/geometry/setRmin          0.00 cm
/gate/Det1/geometry/setRmax          1.00 cm
/gate/Det1/geometry/setHeight        0.50 mm
/gate/Det1/placement/setTranslation  0.00  0.00 -5.10 cm
/gate/Det1/setMaterial Silicon
/gate/Det1/vis/setColor green
/gate/Det1/vis/forceSolid
```

```
#/gate/tel/daughters/name singleDet
#/gate/tel/daughters/insert cylinder
#/gate/singleDet/geometry/setRmin          0.00 cm
#/gate/singleDet/geometry/setRmax          1.00 cm
#/gate/singleDet/geometry/setHeight        0.04 mm
#/gate/singleDet/placement/setTranslation  0.00  0.00  -7.10 cm
#/gate/singleDet/setMaterial Silicon
#/gate/singleDet/vis/setColor green
#/gate/singleDet/vis/forceSolid


#------------------oooooOOOOO00000OOOOOooooo-------------------#
#                                                             #
#        S E N S I T I V E   D E T E C T O R           #
#                                                             #
#                                                             #
#------------------oooooOOOOO00000OOOOOooooo-------------------#


#
# Crystal SD
#

/gate/systems/SPECThead/crystal/attach tel
#/gate/gas/attachCrystalSD
/gate/Det1/attachCrystalSD
#/gate/singleDet/attachCrystalSD


#
# Phantom SD
#
# /gate/P0/attachPhantomSD
# /gate/P1/attachPhantomSD
# /gate/P2/attachPhantomSD
# /gate/Collimator/attachPhantomSD


#------------------oooooOOOOO00000OOOOOooooo-------------------#
#                                                             #
#  D E F I N I T I O N   A N D   D E S C R I T I O N    #
#      O F   Y O U R   P H Y S I C S              #
#                                                             #
#------------------oooooOOOOO00000OOOOOooooo-------------------#

#    EM P R O C E S S

#/gate/physics/gamma/selectRayleigh lowenergy
#/gate/physics/gamma/selectPhotoelectric lowenergy
#/gate/physics/gamma/selectCompton lowenergy

#I N A C T I V E   S E C O N D A R Y   E L E C T R O N S

# /gate/physics/setElectronCut 100 m


#I N A C T I V E   X - R A Y S

# /gate/physics/setXRayCut 1. GeV
# /gate/physics/setDeltaRayCut 1. GeV
```

```
#-------------------oooooOOOOO00000OOOOOooooo--------------------#
#                                                                #
#   I N I T I A L I Z A T I O N   O F   Y O U R                  #
#         S I M U L A T I O N                                    #
#                                                                #
#-------------------oooooOOOOO00000OOOOOooooo--------------------#


/gate/geometry/enableAutoUpdate
/run/initialize


#-------------------oooooOOOOO00000OOOOOooooo--------------------#
#                                                                #
# D E F I N I T I O N   O F   Y O U R   A C Q U I S I T I O N    #
# D I G I T I Z E R   &   C O I N C I D E N C E   S H O R T E R  #
#                                                                #
#-------------------oooooOOOOO00000OOOOOooooo--------------------#


/gate/output/digi/enable


#A D D E R
/gate/digitizer/Singles/insert adder

#     R E A D O U T
# /gate/digitizer/Singles/insert readout
# /gate/digitizer/Singles/readout/setDepth 1


#    E N E R G Y   B L U R R I N G
/gate/digitizer/Singles/insert blurring
/gate/digitizer/Singles/blurring/setResolution 0.075
/gate/digitizer/Singles/blurring/setEnergyOfReference 662. keV


#    E N E R G Y   C U T
# /gate/digitizer/Singles/insert thresholder
# /gate/digitizer/Singles/thresholder/setThreshold 50. keV
# /gate/digitizer/Singles/insert upholder
# /gate/digitizer/Singles/upholder/setUphold 250. keV


#-------------------oooooOOOOO00000OOOOOooooo--------------------#
#                                                                #
#         D E F I N I T I O N   O F                             #
#         Y O U R   O U T P U T   F I L E                        #
#                                                                #
#-------------------oooooOOOOO00000OOOOOooooo--------------------#


/gate/output/analysis/enable
/gate/output/ascii/enable
/gate/output/root/disable
/gate/output/projection/disable
/gate/output/interfile/disable


# /gate/output/sinogram/disable
# /gate/output/ecat7/disable
# /gate/output/lmf1/disable
```

```
#    C H A N G E   T H E    S E E D (1) O R   N O T (0)
# /gate/output/root/setSaveRndmFlag 1


#     S E T U P  - R O O T  F I L E
# /gate/output/root/setFileName YourSPECTSimu
# /gate/output/root/setRootSinglesAdderFlag 0
# /gate/output/root/setRootSinglesBlurringFlag 0
# /gate/output/root/setRootSinglesThresholderFlag 0
# /gate/output/root/setRootSinglesUpholderFlag 0


#     S E T U P  - A S C I I  F I L E
# /gate/output/ascii/setOutFileSinglesAdderFlag 0
# /gate/output/ascii/setOutFileSinglesBlurringFlag 0
# /gate/output/ascii/setOutFileSinglesThresholderFlag 0
# /gate/output/ascii/setOutFileSinglesUpholderFlag 0
/gate/output/ascii/setOutFileSinglesFlag 1
/gate/output/ascii/setOutFileHitsFlag 1


#    I N T E R F I L E  P R O J E C T I O N
# /gate/output/projection/pixelSizeX 0.904 mm
# /gate/output/projection/pixelSizeY 0.904 mm
# /gate/output/projection/pixelNumberX 128
# /gate/output/projection/pixelNumberY 128
# Specify the projection plane (XY, YZ or ZX)
# /gate/output/projection/projectionPlane YZ


#------------------oooooOOOOO00000OOOOOooooo-------------------#
#                                                              #
#          D E F I N I T I O N   O F                           #
#          Y O U R   V E R B O S I T Y   L E V E L             #
#                                                              #
#------------------oooooOOOOO00000OOOOOooooo-------------------#


/control/verbose 0
#/grdm/verbose 0
/run/verbose 0
/event/verbose 0
/tracking/verbose 0
/gate/application/verbose 0
/gate/generator/verbose 0
/gate/stacking/verbose 0
/gate/event/verbose 0
/gate/source/verbose 0
```

```
#-----------------oooooOOOOO00000OOOOOooooo-------------------#
#                                                             #
#           D E F I N I T I O N   O F                         #
#              Y O U R   S O U R C E S                        #
#                                                             #
#-----------------oooooOOOOO00000OOOOOooooo-------------------#


#       ALPHA SOURCE
/gate/source/addSource Am
/gate/source/Am/gps/type Volume
/gate/source/Am/gps/shape Cylinder
/gate/source/Am/gps/radius   0.15 cm
/gate/source/Am/gps/halfz   0.05 mm
/gate/source/Am/gps/centre   0.00  0.00   -21.75 cm
/gate/source/Am/gps/angtype iso
/gate/source/Am/setActivity  40000. Bq
/gate/source/Am/gps/particle ion
/gate/source/Am/gps/ion 2 4 2 0.0
/gate/source/Am/gps/energytype Mono
/gate/source/Am/gps/energy     5.486 MeV
/gate/source/Am/gps/mintheta   0. deg
/gate/source/Am/gps/maxtheta 180. deg
/gate/source/Am/gps/minphi     0. deg
/gate/source/Am/gps/maxphi   360. deg




#-----------------oooooOOOOO00000OOOOOooooo-------------------#
#                                                             #
#        S T A R T   A C Q U I S I T I O N                    #
#          T I M E   P A R A M E T E R S                      #
#                                                             #
#-----------------oooooOOOOO00000OOOOOooooo-------------------#


#
#    E X P E R I M E N T
#

#/random/setSavingFlag  0
#/random/resetEngineFrom currentEvent.rndm

/gate/application/setTimeSlice   10.00  s
/gate/application/setTimeStart    0.00  s
/gate/application/setTimeStop   840.00  s

/gate/application/startDAQ

#----------#
# E X I T #
#----------#

exit
```

III. Error calculation of the cross section

The cross section is given by the following formula:

$$\sigma = \frac{N\Omega_m \sigma_{Ruth}}{N_m \Omega} \tag{III.1}$$

where

N: is the number of counts of each single detector or telescope,

N_m: is the number of counts of monitor and it is referred to elastic scattering

σ_{Ruth}:   is the Rutherford scattering cross section (is referred to elastic scattering)

Ω: is the solid angle of each single detector or telescope and

Ω_m: is the solid angle of the monitor (is referred to elastic scattering).

So, the error Σ is evaluated applying the error propagation formula:

$$\Sigma = \left[\left(\frac{\partial\sigma}{\partial N}\Sigma_N \right)^2 + \left(\frac{\partial\sigma}{\partial N_m}\Sigma_{N_m} \right)^2 + \left(\frac{\partial\sigma}{\partial\Omega}\Sigma_\Omega \right)^2 + \left(\frac{\partial\sigma}{\partial\Omega_m}\Sigma_{\Omega_m} \right)^2 \right]^{\frac{1}{2}} \tag{III.2}$$

$$= \left[\left(\frac{\Omega_m \sigma_{Ruth}\Sigma_N}{N_m\Omega} \right)^2 + \left(\frac{N\Omega_m \sigma_{Ruth}\Sigma_{N_m}}{N_m^2\Omega} \right)^2 + \left(\frac{N\Omega_m \sigma_{Ruth}\Sigma_\Omega}{N_m\Omega^2} \right)^2 + \left(\frac{N\sigma_{Ruth}\Sigma_{\Omega_m}}{N_m\Omega} \right)^2 \right]^{\frac{1}{2}} =$$

$$= \sigma_{Ruth} \left[\frac{\Omega_m^2 \Sigma_N^2}{N_m^2\Omega^2} + \frac{\Omega_m^2 N^2 \Sigma_{N_m}^2}{N_m^4\Omega^2} + \frac{\Omega_m^2 N^2 \Sigma_\Omega^2}{N_m^2\Omega^4} + \frac{N^2 \Sigma_{\Omega_m}^2}{N_m^2\Omega^2} \right]^{\frac{1}{2}} =$$

$$= \frac{N\Omega_m \sigma_{Ruth}}{N_m\Omega} \left(\frac{\Sigma_N^2}{N^2} + \frac{\Sigma_{N_m}^2}{N_m^2} + \frac{\Sigma_\Omega^2}{\Omega^2} + \frac{\Sigma_{\Omega_m}^2}{\Omega_m^2} \right)^{\frac{1}{2}} \Rightarrow$$

$$\Rightarrow \Sigma = \sigma \left(\frac{\Sigma_N^2}{N^2} + \frac{\Sigma_{N_m}^2}{N_m^2} + \frac{\Sigma_\Omega^2}{\Omega^2} + \frac{\Sigma_{\Omega_m}^2}{\Omega_m^2} \right)^{\frac{1}{2}} \tag{III.3}$$

However,

$$\Sigma_N^2 = \left(\sqrt{N} \right)^2 = N \tag{III.4}$$

and

$$\Sigma_{N_m}^2 = \left(\sqrt{N_m} \right)^2 = N_m \tag{III.5}$$

Therefore:

$$\Sigma = \sigma \left(\frac{1}{N} + \frac{1}{N_m} + \frac{\Sigma_\Omega^2}{\Omega^2} + \frac{\Sigma_{\Omega_m}^2}{\Omega_m^2} \right)^{1/2}$$

(III.6)

On the other hand, the solid angle Ω is calculated from alphas radiation formula:

$$\Omega = \frac{4\pi N_\alpha}{Rt}$$

(III.7)

where:

N_α: is the counts from α source (Americium),

R: is the radioactivity of alphas source (40kBq) and

t: is the record time

The most important errors in this formula are introduced from the N_α (statistic error $= \Sigma_\alpha = N_\alpha^{1/2}$) and from the time ($\Sigma_t = \pm 30$ sec).

So,

$$\Sigma_\Omega = \left[\left(\frac{\partial \Omega}{\partial N_\alpha} \Sigma_\alpha \right)^2 + \left(\frac{\partial \Omega}{\partial t} \Sigma_t \right)^2 \right]^{1/2}$$

(III.8)

that leads to:

$$\Sigma_\Omega = \left[\left(\frac{4\pi}{Rt} \Sigma_\alpha \right)^2 + \left(\frac{4\pi N_\alpha}{Rt^2} \Sigma_t \right)^2 \right]^{1/2} =$$

$$= \frac{4\pi}{Rt} \left[\left(\Sigma_\alpha \right)^2 + \left(\frac{N_\alpha}{t} \Sigma_t \right)^2 \right]^{1/2} =$$

$$= \frac{4\pi}{Rt} \left[N_\alpha + \frac{N_\alpha^2}{t^2} \Sigma_t^2 \right]^{1/2} = \frac{4\pi}{Rt} \left[N_\alpha + \frac{N_\alpha^2}{t^2} \Sigma_t^2 \right]^{1/2} \Rightarrow$$

$$\Rightarrow \Sigma_\Omega = \frac{4\pi}{Rt} \left[N_\alpha \left(1 + \frac{N_\alpha}{t^2} \Sigma_t^2 \right) \right]^{1/2}$$

(III.9)

$$\frac{\Sigma_\Omega^2}{\Omega^2} = \frac{\left(\frac{4\pi}{Rt} \left[N_\alpha \left(1 + \frac{N_\alpha}{t^2} \Sigma_t^2 \right) \right]^{1/2} \right)^2}{\left(\frac{4\pi N_\alpha}{Rt} \right)^2} = \frac{N_\alpha \left(1 + \frac{N_\alpha}{t^2} \Sigma_t^2 \right)}{N_\alpha^2} \Rightarrow$$

$$\Rightarrow \frac{\Sigma_\Omega^2}{\Omega^2} = \frac{t^2 + N_\alpha \Sigma_t^2}{t^2 N_\alpha}$$

(III.10)

In the same way, the last term of the (III.3) is given by the formula below:

$$\frac{\Sigma^2_{\Omega_m}}{\Omega^2_m} = \frac{t_m^2 + N_{\alpha m}\Sigma_t^2}{t_m^2 N_{\alpha m}} \tag{III.11}$$

Finally:

$$\Sigma = \sigma \left[\frac{1}{N} + \frac{1}{N_m} + \frac{t^2 + N_\alpha \Sigma_t^2}{t^2 N_\alpha} + \frac{t_m^2 + N_{\alpha m}\Sigma_t^2}{t_m^2 N_{\alpha m}} \right]^{1/2} \tag{III.12}$$

IV. Routine in *C*: Lab to C.M converter

The following program, in *C* language, was used in the data analysis in order to convert the transfer reaction cross sections from the lab system to the center of mass system.

<u>Input file</u>

```c
# include<stdio.h>
# include<stdlib.h>
# include<math.h>


int main(void)  {

  int i;
  float a[12],b[12],q[12],y[12],E3[12],g[12],s[12];
  float thetacm[12],sigmacm[12],c[12],d[12], costhcm[12];
  float thetalab,sigmalab,M1,M2,M3,M4,Q,ET,E1,E2;
  float A,B,C,D,M,m1,m2,m3,m4;

   printf(" Please enter the mass of the projectile in amu:\n");
   scanf("%f", &m1);
   printf("\n");
   printf(" Please enter the mass of the target in amu:\n");
   scanf("%f", &m2);
   printf("\n");
   printf(" Please enter the mass of the light product in amu:\n");
   scanf("%f", &m3);
   printf("\n");
   printf(" Please enter the mass of the heavy product in amu:\n");
   scanf("%f", &m4);
   printf("\n");
   printf(" Please enter the energy of the reaction in MeV: \n");
   scanf("%f", &E1);

   M1=931.478*m1;
   M2=931.478*m2;
   M3=931.478*m3;
   M4=931.478*m4;
   Q=M1+M2-M3-M4;
   ET=E1+Q;
   M=(M1+M2)*(M3+M4);
   A=(M1*M4*(E1/ET))/M;
   B=(M1*M3*(E1/ET))/M;
   C=(M2*M3*(1+(M1*Q/(M2*ET))))/M;
   D=(M2*M4*(1+(M1*Q/(M2*ET))))/M;
```

```c
struct oxygen  {
     float thetalab;
     float sigmalab;
}list[12];

 FILE *fp;
fp=fopen("input.txt","r");

printf("\n");
printf("\n");
printf("\n");
printf("\n");
printf("\n");

  printf("thetaLAB      thetaCM      sigmaLAB      sigmaCM\n");
   for(i=0;i<12;i++) {
   fscanf(fp,"%f %f", &list[i].thetalab, &list[i].sigmalab);
   b[i]=list[i].thetalab;
   y[i]=3.14159*b[i]/180 ;
   a[i]=cos(y[i]);
   c[i]=(pow(sin(y[i]),2.));
   d[i]=sqrt((D/B)-c[i]);
   g[i]=(a[i]+d[i])*(a[i]+d[i]);
   E3[i]=B*ET*g[i];

   costhcm[i]=((E3[i]/ET)-B-D)/(2*sqrt(A*C));
   s[i]=acos(costhcm[i]);
   thetacm[i]=s[i]*180./3.14159;
   sigmacm[i]=list[i].sigmalab*((sqrt(A*C))*(sqrt((D/B)-(pow(sin(y[i]),2.)))))/(E3[i]/ET);

   printf("%4.0f %15.1f %15.4f %15.6f\n",list[i].thetalab, thetacm[i], list[i].sigmalab,
sigmacm[i]);
}

     fclose(fp);
     return 0;
 }
```

V. Tables

Table V1: _Results of the pulser calibration through an alpha source._

$$\text{Pulser} = A_0 + A_1X + A_2X^2 + A_3X^3 + A_4X^4 + A_5X^5, \; X=\text{Channel}$$

Detector Telescope	A_0	A_1	A_2	A_3	A_4	A_5	alpha peak (Channel)	alpha peak (Pulser)
M1	-5.27E-03	8.13E-04	4.69E-10	5.25E-13	-1.74E-16	1.43E-20	300.00	0.23874
M2	-3.72E-03	7.79E-04	7.09E-09	-2.23E-12	3.40E-16	-1.96E-20	316.70	0.24363
S1	-4.15E-03	9.94E-04	6.53E-09	-2.31E-12	3.62E-16	-2.08E-20	247.00	0.24163
S2	-2.33E-03	8.88E-04	3.75E-09	-9.74E-13	1.15E-16	-4.76E-21	262.00	0.23069
S3	-3.79E-03	9.13E-04	3.47E-09	-8.06E-13	8.05E-17	-2.53E-21	266.00	0.23926
S4	-5.58E-04	9.55E-04	4.63E-09	-1.45E-12	2.08E-16	-1.10E-20	246.00	0.23474
S5	-3.82E-05	1.11E-03	9.09E-09	-4.86E-12	1.24E-15	-1.16E-20	224.00	0.24901
S6	-4.73E-03	8.79E-04	4.48E-09	-1.38E-12	1.86E-16	-9.28E-21	254.00	0.21887
S7	-4.81E-03	9.20E-04	-1.12E-09	5.55E-13	-1.05E-16	6.67E-21	246.50	0.22192
T1-E	-3.81E-03	1.04E-03	5.04E-09	-1.45E-12	2.01E-16	-1.08E-20	218.00	0.22313
T2-E	-3.71E-03	9.67E-04	4.85E-09	-1.53E-12	2.03E-16	-9.80E-21	234.00	0.22282
T3-E	-3.12E-03	1.03E-03	3.84E-09	-1.03E-12	1.22E-16	-5.76E-21	210.00	0.21334
T1-ΔE	1.24E-04	3.52E-05	5.69E-10	-8.15E-14	2.24E-18	2.49E-22	342.00	0.01223
T2-ΔE	-5.92E-03	5.14E-05	-7.85E-09	2.20E-12	-2.76E-16	1.28E-20	330.00	0.01027
T3-ΔE	-2.23E-03	3.82E-05	-1.95E-09	5.46E-13	-7.04E-17	3.41E-21	358.00	0.01123

Table V2*: Results of the energy calibration for all the detectors. The energy occurs to be a linear function of the channel.*

	Energy= B*Channel + C	
Detector	**B**	**C**
M1	0.01876	-0.16025
M2	0.01779	-0.1849
S1	0.02273	-0.1432
S2	0.02128	-0.11858
S3	0.02107	-0.14598
S4	0.02248	-0.08169
S5	0.02463	-0.01486
S6	0.02218	-0.16673
S7	0.02273	-0.11596
T1-E	0.0236	-0.14988
T2-E	0.02194	-0.11551
T3-E	0.02429	-0.10452
T1-ΔE	0.00139	-0.05128
T2-ΔE	0.00177	-0.01067
T3-ΔE	0.00144	-0.02364

Table V3*: Results of the identification procedure for the $^{28}Si(^{20}Ne,^{16}O)^{32}S$ reaction at 52.3 MeV. The experimental energy values, denoted as E_{exper} , are compared with the predicted ones labeled as E_{pred}.*

Target position	**Θ_{lab}(degrees)**	**Telescope**	**E_{exper}(MeV)**	**E_{pred}(MeV)**	**Variation**
Vertical (200 µg/cm^2)	25	T1-E	44.80	44.80	0.00%
	50	T1-E	24.05	30.30	-20.63%
	60	T1-E	19.34	23.60	-18.05%
Tilted by 30° (200 µg/cm^2)	27	T1-E	38.96	43.50	-10.44%
	33	T1-E	38.55	40.30	-4.34%
	47	T2-E	25.13	32.47	-22.61%
	50	T2-E	21.00	30.55	-31.26%

Table V4: *Results of the identification procedure for the $^{28}Si(^{20}Ne,^{16}O)^{32}S$ reaction at 70 MeV. The experimental energy values, denoted as E_{exper}, are compared with the predicted ones labeled as E_{pred}.*

Target position	Θ_{lab}(degrees)	Telescope	E_{exper}(MeV)	E_{pred}(MeV)	Variation
	25	T1-E	58.04	63.24	-8.22%
	30	T1-E	53.14	59.96	-11.38%
	35	T1-E	49.26	56.26	-12.44%
Vertical	40	T1-E	47.83	52.27	-8.50%
(200 µg/cm^2)	45	T1-E	47.46	48.01	-1.14%
	40	T2-E	49.34	52.27	-5.61%
	45	T2-E	40.37	48.01	-15.91%
	50	T2-E	40.50	43.64	-7.20%

Table V5: *Results of the identification procedure for the $^{28}Si(^{20}Ne,^{24}Mg)^{24}Mg$ reaction at 52.3 MeV. The experimental energy values, denoted as E_{exper}, are compared with the predicted ones labeled as E_{pred}.*

Target position	Θ_{lab} (degrees)	Telescope	E_{exper}(MeV)	E_{pred}(MeV)	Variation
Vertical	37	T2-E	27.13	25.54	6.23%
(200 µg/cm^2)	40	T2-E	26.26	22.82	15.07%
Tilted by 30° (200 µg/cm^2)	47	T2-E	19.70	16.80	17.26%

Table V6: *Results of the identification procedure for the $^{28}Si(^{20}Ne,^{24}Mg)^{24}Mg$ reaction at 70 MeV. The experimental energy values, denoted as E_{exper}, are compared with the predicted ones labeled as E_{pred}.*

Target position	Θ_{lab} (degrees)	Telescope	E_{exper}(MeV)	E_{pred}(MeV)	Variation
	30	T1-E	46.81	47.76	-1.99%
	35	T1-E	38.91	42.55	-8.55%
	40	T1-E	34.97	36.92	-5.27%
Vertical	45	T1-E	27.18	31.03	-12.40%
(200 µg/cm^2)	45	T2-E	21.08	31.03	-32.06%
	50	T1-E	17.97	24.99	-28.09%
	50	T2-E	14.43	24.99	-42.26%
Tilted by 30°	55	T1-ΔE	8.53	9.05	-5.79%
(200 µg/cm^2)	55	T2-ΔE	11.62	9.05	28.34%
	60	T2-E	5.85	13.36	-56.20%

Table V7: *Results of the identification procedure for the $^{28}Si(^{20}Ne,^{12}C)^{36}Ar$ reaction at 52.3 MeV. The experimental energy values, denoted as E_{exper}, are compared with the predicted ones labeled as E_{pred}.*

Target position	Θ_{lab}(degrees)	Telescope	E_{exper}(MeV)	E_{pred}(MeV)	Variation
Vertical (200 µg/cm²)	37	T2-E	33.88	41.10	-17.57%
	40	T2-E	32.88	39.67	-17.12%
	55	T1-E	25.04	31.81	-21.28%
Vertical (130 µg/cm²)	30	T1-E	38.10	44.50	-14.38%
	35	T1-E	34.01	42.33	-19.66%
	40	T2-E	36.57	39.99	-8.55%
	45	T2-E	34.79	37.46	-7.13%
Tilted by 30° (200 µg/cm²)	27	T1-E	37.77	45.19	-16.42%
	33	T1-E	33.53	42.65	-21.38%
	47	T2-E	32.09	36.21	-11.38%
	50	T2-E	31.45	34.65	-9.24%
	55	T2-E	32.54	32.00	1.69%

Table V8: *Results of the identification procedure for the $^{28}Si(^{20}Ne,^{12}C)^{36}Ar$ reaction at 70 MeV. The experimental energy values, denoted as E_{exper}, are compared with the predicted ones labeled as E_{pred}.*

Target position	Θ_{lab}(degrees)	Telescope	E_{exper}(MeV)	E_{pred}(MeV)	Variation
Vertical target (200 µg/cm²)	25	T1-E	63.36	64.22	-1.34%
	35	T1-E	57.41	58.67	-2.15%
	40	T2-E	44.22	55.45	-20.25%
	45	T1-E	49.13	52.04	-5.59%
	50	T1-E	41.60	48.47	-14.18%
	50	T2-E	35.89	48.47	-25.96%